Editors' Suggestion

Bulk localized transport states in infinite and finite quasicrystals via magnetic aperiodicity

Dean Johnstone,[1,*,†] Matthew J. Colbrook,[2,3,*,‡] Anne E. B. Nielsen,[4,5] Patrik Öhberg,[1] and Callum W. Duncan[6,4,§]

[1]*SUPA, Institute of Photonics and Quantum Sciences, Heriot-Watt University, Edinburgh EH14 4AS, United Kingdom*

[2]*Department of Applied Mathematics and Theoretical Physics, University of Cambridge, Wilberforce Road, Cambridge CB3 0WA, United Kingdom*

[3]*Centre Sciences des Données, École Normale Supérieure, 45 rue d'Ulm, 75005 Paris, France*

[4]*Max-Planck-Institut für Physik komplexer Systeme, D-01187 Dresden, Germany*

[5]*Department of Physics and Astronomy, Aarhus University, DK-8000 Aarhus C, Denmark*

[6]*Department of Physics and SUPA, University of Strathclyde, Glasgow G4 0NG, United Kingdom*

(Received 6 August 2021; revised 13 June 2022; accepted 6 July 2022; published 29 July 2022)

Robust edge transport can occur when charged particles in crystalline lattices interact with an applied external magnetic field. Such systems have a spectrum composed of bands of bulk states and in-gap edge states. For quasicrystalline systems, we still expect to observe the basic characteristics of bulk states and current-carrying edge states. We show that, for quasicrystals in magnetic fields, there is an additional third option—bulk localized transport (BLT) states. BLT states share the in-gap nature of the well-known edge states and can support transport, but they are fully contained within the bulk of the system, with no support along the edge. Thus, transport is possible along the edge and within distinct regions of the bulk. We consider both finite-size and infinite-size systems, using rigorous error controlled computational techniques that are not prone to finite-size effects. BLT states are preserved for infinite-size systems, in stark contrast to edge states. This allows us to observe transport in infinite-size systems, without any perturbations, defects, or boundaries being introduced. We confirm the in-gap topological nature of BLT states for finite- and infinite-size systems by computing the Bott index and local Chern marker (common topological measures). BLT states form due to magnetic aperiodicity, arising from the interplay of lengthscales between the magnetic field and the quasiperiodic lattice. BLT could have interesting applications similar to those of edge states, but now taking advantage of the larger bulk of the lattice. The infinite-size techniques introduced here, especially the calculation of topological measures, could also be widely applied to other crystalline, quasicrystalline, and disordered models.

DOI: 10.1103/PhysRevB.106.045149

I. INTRODUCTION

In crystalline materials, e.g., condensed matter or cold atoms in optical lattices, the standard picture according to band theory is that a system is either an insulator or metal [1,2]. During the 1980s, this picture began to change with the discovery of topological states of matter [3–5]. For example, topological edge states (ESs) can occur when a charged particle in a crystal interacts with an external magnetic field [6,7]. The physics of charged particles in a two-dimensional crystalline lattice with an applied strong magnetic field is a well-studied problem for both the single-particle [8–14] and many-body [15–18] regimes. There have also been numerous experimental realizations and proposals [7,19–22].

Quasicrystals, on the other hand, have short-range disorder and long-range order [23–27]. This makes their features distinct from both periodic and disordered lattices. The general electronic properties of quasicrystals are little understood, especially in comparison to their periodic counterparts [26,28]. Two-dimensional quasicrystalline systems have been proposed and now experimentally realized to varying degrees in ultracold atoms [29–32], graphene bilayers [33], and photonics [34–36].

Recently, there has been renewed interest in adding a magnetic field to scenarios involving quasicrystalline lattices [37–43]. In quasicrystals, the concepts of bands and band gaps are difficult to consistently define since Bloch's theorem is not enforceable without approximations to the overall structure. While recent results have confirmed the presence of ESs in a magnetic field [38,43] and studied the appearance of higher-order topological states [44–46] in quasicrystals, there have been few tangible differences from their study in periodic systems.

In this paper, we show that the common picture of insulators, metals, and topological insulators with surface states is not the full story for quasiperiodic systems. When the

*These authors contributed equally to this work.
†dj79@hw.ac.uk
‡m.colbrook@damtp.cam.ac.uk
§callum.duncan@strath.ac.uk

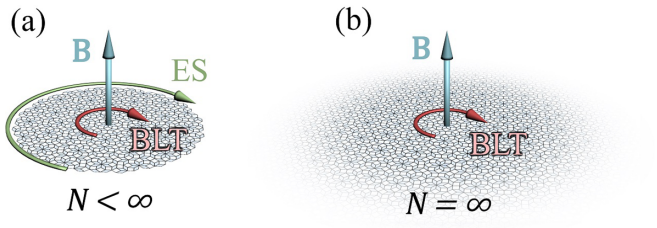

FIG. 1. Illustration of the different types of in-gap states in (a) finite and (b) infinite quasicrystals when a uniform magnetic field (blue arrow) is present. In the case of a finite quasicrystal with N sites (a), the green arrow depicts potential transport across a conventional ES, which forms at the boundaries of the lattice. The quasicrystal may also permit the formation of BLT, whose potential transport is depicted by the red arrow. In the case of a truly infinite quasicrystal (b), we no longer have boundaries and hence no ES, but we retain the BLT state and its supported transport.

confining potential is quasicrystalline, there are multiple competing, not necessarily commensurate, lengthscales arising from the magnetic field and quasiperiodic lattice. This results in a magnetic aperiodicity, directly leading to the observation of *bulk localized transport* (BLT) states. As BLT states arise from the magnetic aperiodicity, they are significantly different from previous states found in the internal sections of fractal lattices [47–49]. Such fractal lattices are almost entirely composed of effective hard edges with no discernible bulk, meaning these "internal" ESs are conventional ESs on an unconventional lattice. In contrast, BLT states are not an artefact of effective edges introduced through an impurity or set of dislocations [13,50–58]. BLT states also have a different character from zero-dimensional corner modes found in quasicrystals [44] that are bound to corners on the hard boundary of a finite system. BLT states do share many of the properties of ESs, but they are entirely localized within the bulk, as illustrated in Fig. 1. Importantly, BLT states support transport (or currents) in the same way as the well-studied ESs, making them useful for future applications.

A. Overview

Before detailing our methods, we present an overview of the main results of our work. This section is intended to review our work, with references to the rest of this paper, where we discuss the approach and results in detail.

Quasicrystals and magnetic fields. We envisage a system of charged particles existing on a quasicrystalline lattice under the influence of a uniform perpendicular magnetic field. This system is illustrated in Fig. 1. The Hamiltonian of this system is well described by the Hofstadter vertex model, introduced in Sec. II, which modifies the standard Hofstadter model to the vertex model of a quasicrystalline tiling, illustrated in Fig. 2. Solving for the finite-size spectrum and states of the Hofstadter vertex model is straightforward. However, defining bands and in-gap states is difficult due to the breakdown of Bloch's theorem. We define the in-gap states, and hence the bands, via topological measures that are nonzero for in-gap states and outlined in Sec. III.

Infinite-size quasicrystals. The states we consider are supported by the bulk of the lattice, and hence we consider if they

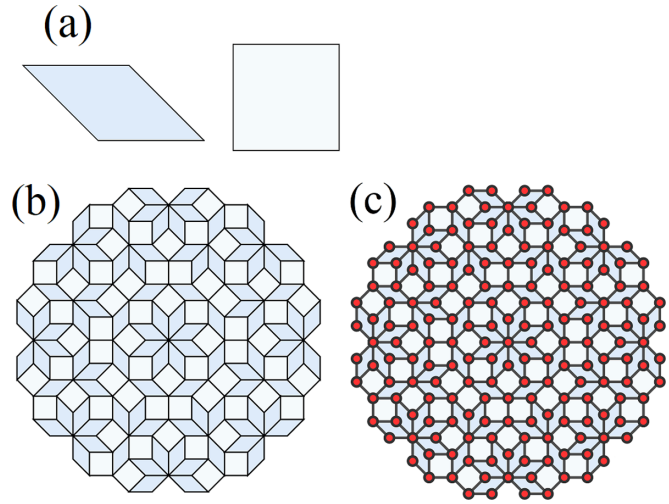

FIG. 2. Construction of the Ammann–Beenker (AB) tiling, using the (a) incommensurate square and rhombus as prototiles. The aperiodic tiling is generated from these prototiles, leaving no gaps. Here, we take a circular cutoff in tiling space to show (b) a finite sample of AB tiling and preserve rotational symmetry with respect to the origin (center of the tiling). The corresponding vertex model (c) is defined by setting bonds as the edges of tiles, and the lattice sites as the intersection of tile edges. In this example, the total number of lattice sites is $N = 185$.

are retained in the spectrum of the infinite Hamiltonian. To deal with the infinite-size quasicrystalline lattice, we utilize an infinite-size error controlled algorithm that abandons square truncation (of infinite matrix representations) to account for the interaction of sites outside a finite patch of the lattice. The infinite-size algorithm is described in Sec. II B, and it can be utilized to calculate the spectrum of other infinite-dimensional operators [59]. We also detail a new extension of the infinite-size algorithm to calculate topological measures, as described in Sec. III A. This allows us to identify states with in-gap characteristics in the infinite-size quasicrystal (or any crystal or aperiodic lattice).

BLT states. We first illustrate BLT states in Sec. IV by considering the Hofstadter vertex model of the quasicrystalline Ammann-Beenker (AB) tiling. As already stated, BLT states are peculiar as they are in-gap, yet entirely localized within the bulk of the lattice, with no component on the edge. Examples of BLT states are given for the AB tiling in Figs. 4(c) and 7, clearly illustrating the bulk nature of these in-gap states. BLT states are also shown to be in-gap from their nonzero topological measures. Interestingly, the proportion of states that are of BLT-type in a finite system converges to a nonzero value with increasing system size, as shown in Fig. 6. This is contrary to regular ESs, which become a vanishingly small proportion of the states with increasing system size. As expected from the arguments illustrated in Fig. 1, we find that BLT states exist in the infinite-size spectrum, and they are of the same character as those in the finite system; see Fig. 9 for examples. Furthermore, in Sec. IV D we consider offset tilings, and we find that the BLT states persist in the spectra even if the rotational symmetry of the quasicrystal is broken, and that nearly degenerate BLT states exist throughout the quasicrystal on self-similar sections.

Supported bulk transport. Key to the future consideration and application of BLT states is the fact that they support transport like any other in-gap state. This results in BLT, which is independent of the existence or form of any edges. In this way, BLT can be considered to be robust against perturbations along the edge, much like regular edge states are robust against perturbations in the bulk. We explicitly show that transport is supported by the BLT states of the AB Hofstadter vertex model in both the finite- and infinite-size cases in Figs. 15 and 16, respectively. We also show that the location of this transport can be varied due to BLT states being supported on different parts of the bulk.

B. Terminology

As this work straddles condensed matter, quantum simulators, and spectral computations from mathematical physics, there are specific terminologies we need to define to avoid confusion for readers of different fields.

First, we refer to a lattice as periodic or crystalline as long as a unit cell can be defined with an associated Brillouin zone. Bloch's theorem can then be used to calculate the band structure of the lattice. This does not exclude the presence of edge states, as they are dependent on the boundary. Even in the case of open boundaries, bands can still be calculated. Therefore, a periodic lattice is defined independently of the boundary conditions (which are usually periodic, infinite, or open). The strict definition of a lattice itself can be considered to apply only to periodic systems. However, the definition of a lattice in condensed matter physics is more general and can be interpreted as defining a group of discrete connected points. We follow this convention and refer to lattices as being any group of discrete connected points throughout this work.

We often refer to bulk states and in-gap states. According to Bloch's theorem, bulk states are all states that are allowed in the system with real quasimomentum. In-gap states are all other solutions to the Schrödinger equation for the lattice Hamiltonian, which are the complex quasimomentum solutions [13]. In general, we do not have access to the quasimomentum from numerical approaches. As Bloch's theorem breaks down in quasicrystals, we must turn to alternative methods to define if a state of the spectrum is in-gap. For this, we turn to the topological measures of the Bott index and local Chern marker, discussed in Sec. III A.

The meaning of an edge state must also be clearly defined. In spectral computational problems of operators on infinite-dimensional spaces (in our case, corresponding to the infinite-size lattice), one of the main problems is the removal of spectral pollution. Spectral pollution refers to a set of states in the spectrum that are not actually part of the infinite-size spectrum. These typically manifest in the form of edge states due to finite-size effects. While the edge states do not exist in the spectrum of infinite-size operators, they are physical states of the finite-size system, with distinct observable properties. Note, the BLT states outlined in this paper are not spectral pollution—they are part of the spectrum of the infinite-size operator, as shown in Sec. IV B. This means that not all in-gap states are spectral pollution, as is usually thought.

II. MODELS OF QUASICRYSTALS IN MAGNETIC FIELDS

A. Hofstadter vertex model

We consider lattices generated from the vertex model of aperiodic tilings. A 2D tiling is a countable family of closed sets (prototiles) which covers the entire 2D plane without any gaps or overlaps [26,60,61]. Aperiodic tilings are a subclass of tilings that exhibit long-range order, but no short-range translational invariance. Finding tiles that enforce quasiperiodicity is not a simple task, and the initial aperiodic tiling patterns contained thousands of distinct tiles [26]. Penrose discovered an aperiodic tiling requiring only a few rhombic tiles [62]. Since then, a multitude of aperiodic tilings have been discovered with a variety of noncrystalline rotational symmetries [26,63]. We focus on an AB vertex model as an example, which may be generated from an incommensurate rotation and projection of the 4D hypercubic lattice [64–66]. We illustrate the quasicrystalline AB vertex model and its construction from an aperiodic tiling in Fig. 2. However, our results are not specific to this 8-fold tiling, and we will show that BLT can occur in other quasicrystalline lattices in Appendix B.

The vertex model considers a lattice site at each vertex of the aperiodic tiling and bonds along the edges of tiles [67–70], as shown in Figs. 2(b) and 2(c). We consider the vertex model of the AB tiling with a perpendicular constant magnetic field, as depicted in Fig. 1. The single-particle Hamiltonian is then

$$H = -J \sum_{\langle j,k \rangle}^{N} e^{i\theta_{jk}} |j\rangle\langle k|, \tag{1}$$

where θ_{jk} is the Peierls phase [71] due to the magnetic field between sites j and k, $\langle j,k \rangle$ is the sum over all N vertices/sites connected by an edge, and $|j\rangle$ is the state of a particle occupying site j. We consider the Landau gauge $\mathbf{A}(\mathbf{r}) = Bx\hat{\mathbf{y}} = (\phi/A)x\hat{\mathbf{y}}$, with the magnetic field strength B, flux ϕ (measured in terms of the flux quantum $\phi_0 = 2\pi$), and penetrating area A. We take the area A to be that of the square tile of the AB tiling (the qualitative results, including the observation of BLT states, are independent of the choice of A). Units of $\hbar = e = 1$ are considered throughout this work, and we work in units of energy J. The Hamiltonian Eq. (1) is well-understood when applied to periodic systems [8], and it can even result in similar physics when applied to some quasicrystals [38–40,43,72]. It even exhibits noncrystalline topological properties at high flux [73].

B. Infinite-size algorithm

To rigorously probe the spectral properties of the infinite tiling directly, as opposed to a finite truncation, we use a set of new computational techniques for infinite-dimensional spectral problems [74]. We begin with a description of computing the spectrum, with further details presented in Appendix A. As an example, the results of the infinite algorithm are shown for an infinite square lattice with a Hamiltonian of Eq. (1) in Fig. 3. The algorithm perfectly replicates the fractal Hofstadter butterfly usually generated through the consideration of periodic boundary conditions [8]. The removal of ESs, or in this case spectral pollution (of the infinite tile), can be seen

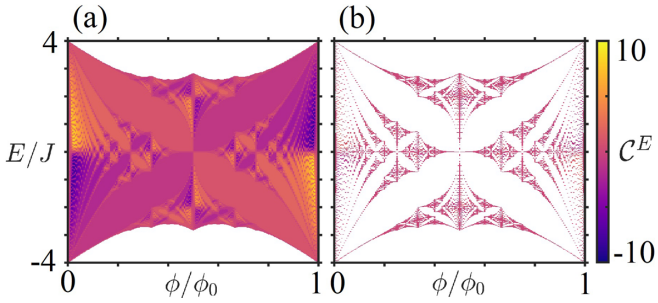

FIG. 3. Obtaining the Hofstadter butterfly for the infinite square lattice from the infinite-size algorithm discussed in Sec. II B. We show the effective Chern marker, defined in Sec. III A, for each state, showing the $\mathcal{C}^E$ (a) over a full range of energy values E, which includes states that are considered to be spectral pollution, and (b) over the infinite-size square lattice Hofstadter butterfly, with a restricted range of energy values in the spectrum of the infinite lattice (up to the specified tolerance 0.01).

by the difference between Figs. 3(a) and 3(b). As discussed previously, spectral pollution is the terminology used to describe spurious eigenvalues that form in gaps of the essential spectrum of the infinite-dimensional operator.

We utilize an algorithm, developed by one of the authors [59], that allows for the calculation of the spectrum of a full infinite-dimensional operator with error control. This algorithm is general in its applications and will be of use in physical scenarios other than that considered here. For example, extensions to unbounded operators and partial differential operators can be found in Ref. [75], and geometric features of spectra can be found in Ref. [76]. For the present paper, the algorithm is of particular use since (i) the aperiodic nature of quasicrystals makes it a considerable challenge to approximate the spectrum of the full infinite-dimensional operator without finite-size effects, and (ii) the approximation error can be computed and reaches effectively zero from a physical standpoint, as detailed below. There has also been an approach developed to obtain the exact solutions of quasicrystals of infinite size through the use of a superspace [77]. This method is specifically constructed to handle quasicrystalline problems by converting them to higher-dimensional periodic problems, and it could be applied in the scenarios discussed in this work. However, we find the algorithm of Ref. [59] to be highly efficient at handling the problem of a quasicrystal of infinite size in a uniform magnetic field.

In infinite dimensions, which in our case corresponds to an infinite tile, the Hamiltonian H can be represented by an infinite Hermitian matrix, $\hat{H} = \{\hat{H}_{ij}\}_{i,j\in\mathbb{N}}$, which acts on $l^2(\mathbb{N})$, the space of square summable sequences. A suitable ordering of the sites (e.g., by positional radius from an origin) leads to a matrix $\hat{H}$ with finitely many nonzero entries in each column. In other words, we have access to a function $f : \mathbb{N} \to \mathbb{N}$ such that $\hat{H}_{ij} = 0$ if $i > f(j)$, thus describing the sparsity of $\hat{H}$. Sparse Hamiltonians are a subclass of operators that are dealt with in Ref. [59] by considering the function

$$F_n(z) := \sigma_{\text{inf}}(P_{f(n)}(\hat{H} - z)P_n),$$

where P_m denotes the orthogonal projection onto the linear span of the first m basis vectors, and σ_{inf} denotes the smallest singular value of the corresponding rectangular matrix. The rectangular truncation $P_{f(n)}(\hat{H} - z)P_n$ corresponds to including all of the interactions of the first n sites (the first n columns of $\hat{H}$) without needing to apply boundary conditions (see, for example, Fig. 1 of [78] and [79]). This is in sharp contrast to standard methods that typically take a square truncation of the matrix $\hat{H}$ (corresponding to a truncation of the tile) with a boundary condition. This difference allows us to prove convergence, provide error control, and lends itself to adaptive computations of the full infinite-dimensional operator. Physically, $F_n(z)$ is the square root of the ground-state energy of the folded Hamiltonian $P_n(\hat{H} - z)^*(\hat{H} - z)P_n$. $F_n(z)$ converges down to the distance of z to the spectrum of H (uniformly on compact subsets of $\mathbb{C}$) as $n \to \infty$ [59]. Together with a local optimization routine, this property leads to the computation of the spectrum and approximate states with error control as $n \to \infty$. Algorithmic steps are provided in Appendix A.

The algorithm's output, $\Gamma_n(H)$, converges to the spectrum $\text{Sp}(H)$ of the full infinite-dimensional operator as $n \to \infty$. Note that this convergence is free from edge states. The error bound of the algorithm satisfies

$$\sup_{z\in\Gamma_n(H)} \text{dist}(z, \text{Sp}(H)) \leqslant E_n$$

for an output E_n that converges to zero as $n \to \infty$. For a desired spectral resolution $\delta > 0$, we simply increase n until $E_n \leqslant \delta$. We stress that this form of error control allows us to guarantee the accuracy of parts of the spectrum that we compute. In other words, we know that the spectra we compute below (e.g., the BLT states) are reliable. However, the algorithm does not tell us whether we have approximated the full spectrum yet (such an algorithm cannot exist without long-range constraints or assumptions on the Hamiltonian), only that we obtain the full spectrum in the limit $n \to \infty$.

III. MEASURES AND PROPERTIES

A. Topological measures

Probing topological invariants in quasicrystalline systems is difficult, due to the ill-defined Brillouin zone and the breakdown of Bloch's theorem. For two-dimensional lattices subject to an external perpendicular magnetic field, the topological invariant of each respective band is its Chern number [6,7]. Differences between Chern numbers of the bands above and below a band gap are then equivalent to the number of ESs that appear within the band gap via the bulk-boundary correspondence. To obtain such topological invariants, integrals are normally taken across the first Brillouin zone of the system [6,80]. This explicitly means that the underlying lattice needs to be crystalline for these integrals to be generic properties of the bulk. However, there are measures that are independent of the boundary and have been shown to be equivalent to properties of the Chern number. We focus on the specific examples of the Bott index [81] and the local Chern marker [82].

1. Finite systems

The Bott index is a spectral quantity defined for each individual state, related to the commutativity of matrices [81,83].

It is defined for the nth eigenstate as

$$\mathcal{B}^n = \frac{1}{2\pi}\mathrm{Im}\{\mathrm{Tr}[\ln(\hat{V}_x^n \hat{V}_y^n \hat{V}_x^{n*} \hat{V}_y^{n*})]\}, \tag{2}$$

with $\hat{V}_{x/y}^n$ being the projected position operators,

$$\hat{V}_x^n = \hat{Q}^n + \hat{P}^n \hat{U}_x \hat{P}^n, \quad \hat{V}_y^n = \hat{Q}^n + \hat{P}^n \hat{U}_y \hat{P}^n,$$

for the nth state cumulative projections

$$\hat{P}^n = \sum_{m=1}^{n} |m\rangle\langle m|, \quad \hat{Q}^n = \hat{\mathbb{I}} - \hat{P}^n, \tag{3}$$

where $|m\rangle$ is the mth eigenstate (we follow the usual convention of listing states in order of increasing eigenvalues), and the unitary diagonal position operators are

$$\hat{U}_x = \exp(2\pi i \hat{x}_S), \quad \hat{U}_y = \exp(2\pi i \hat{y}_S). \tag{4}$$

The $\hat{x}_S/\hat{y}_S$ are position operators that must be scaled between 0 and 1.

By calculating the Bott index, one can measure obstructions to the formation of a maximally localized Wannier basis spanning occupied states [84,85]. To find localized Wannier states, it is usually necessary to find continuous and periodic logarithms of families of unitaries [86]. This is discussed in detail in Ref. [87], where they also show that such logarithms cannot be defined when the Chern numbers associated with the occupied states are nonzero. In essence, the problem boils down to the definition of the fractional power of a matrix and issues around the choice of a branch cut in the complex plane to define the required logarithm [87,88]. Note, this logarithm is not the same as the one utilized in the definition of the Bott index. If at a given energy the Bott index is nonzero, then any state with that energy must be in-gap, as the occupied band of states below must have a nonzero Chern number associated with it. The Bott index has proven useful in disordered and quasicrystalline systems, where bands cannot be defined through Bloch's theorem [41–43,85]. However, it is computationally expensive, as it requires the logarithm of a matrix whose size scales with the lattice. The Bott index does not lend itself to the large system sizes of this work and is, in general, ill-defined in the infinite-size case. Therefore, we turn to an alternative measure—the local Chern marker.

The topological invariant can be projected onto the real physical space of the system. For the Chern number, this gives the local Chern marker [82,89–91]. Unlike the Bott index, local Chern markers are defined on every single site j of the lattice for the nth eigenstate as

$$C_j^n = -4\pi\ \mathrm{Im}\{\langle j|\hat{x}^n \hat{y}^n|j\rangle\}/A_c,$$

with A_c a reference area of the lattice, and

$$\hat{x}^n = \hat{Q}^n \hat{x} \hat{P}^n, \quad \hat{y}^n = \hat{P}^n \hat{y} \hat{Q}^n,$$

where $\hat{x}/\hat{y}$ are the position operators. The local Chern marker has been used to distinguish topological states in quasicrystals and disordered systems [38,92]. For large lattice sizes, we find that the local Chern marker is a more efficient way of distinguishing in-gap states since we do not need to compute a matrix logarithm for each state. Moreover, it can be extended to infinite systems. By taking the integer of maximal counts in the distribution of C_j^n, we consider an effective Chern marker C^n for a given state $|n\rangle$, which we find to be in agreement with the Bott index for crystals and quasicrystals.

2. *Infinite systems*

Associated with the Hamiltonian H is a projection-valued measure, $\mathcal{E}$, whose existence is guaranteed by the spectral theorem [93] and whose support is the spectrum $\mathrm{Sp}(H)$. This diagonalizes H, even when there does not exist a basis of normalizable eigenfunctions (recall that we are working in an infinite-dimensional Hilbert space):

$$H = \int_{\mathrm{Sp}(H)} \lambda d\mathcal{E}(\lambda).$$

In finite dimensions and for compact Hamiltonians, $\mathcal{E}$ consists of a sum of Dirac measures, located at the eigenvalues, whose values are the corresponding projections onto eigenspaces. More generally, however, there may be a continuous component of the spectrum and spectral measure. Generalizations of the spectral projectors in Eq. (3) can be given in terms of $\mathcal{E}$ as

$$\hat{P}^E = \int_{(-\infty,E]} d\mathcal{E}(\lambda), \tag{5}$$

where we now label over energy values E, which also covers the possibility of continuous spectra.

The key ingredient that allows approximations of $\mathcal{E}$ to be computed is the formula for the resolvent,

$$(H - z)^{-1} = \int_{\mathrm{Sp}(H)} \frac{d\mathcal{E}(\lambda)}{\lambda - z}.$$

In Ref. [94], it is shown how to compute the action of the resolvent with error control via the rectangular truncations $P_{f(n)}(\hat{H} - z)P_n$. Using this, we compute a smoothed approximation of $\mathcal{E}$ via convolution with a rational kernel K_ϵ for smoothing parameter $\epsilon > 0$. Taking $z = x + i\epsilon$, the classical example of this is Stone's formula, which corresponds to convolution with the Poisson kernel

$$\frac{1}{2\pi i}[(H - z)^{-1} - (H - \bar{z})^{-1}] = \int_{\mathbb{R}} \frac{\epsilon\pi^{-1}}{(x - \lambda)^2 + \epsilon^2} d\mathcal{E}(\lambda).$$

As $\epsilon \downarrow 0$, this approximation converges weakly (in the sense of measures) to $\mathcal{E}$. However, for a given truncation size, if ϵ is too small, the approximation becomes unstable due to approximating the sum of Dirac measures corresponding to the spectral measure of the truncation of $\hat{H}$. There is an increased computational cost for smaller ϵ, which requires larger truncation parameters. Since we want to approximate spectral properties without finite-size effects, it is advantageous to replace the Poisson kernel with higher-order rational kernels developed in Ref. [95]. This allows a larger ϵ for a given accuracy, thus reducing the computational burden. Through a weighted distribution of resolvents, rational kernels provide us with a generalized Stone formula

$$[K_\epsilon * \mathcal{E}](x) = \frac{-1}{2\pi i}\sum_{j=1}^{m}[\alpha_j(H - (x - \epsilon a_j))^{-1} - \mathrm{c.c.}],$$

which converges with mth order of convergence in ϵ [95,96]. Here, c.c. denotes taking the adjoint, the constants α_j and a_j can be found in Appendix A, and $*$ represents convolution.

With this in hand, and for a given energy value E, we can write down smoothed generalizations of the spectral projectors in Eq. (5) as

$$\hat{P}_\epsilon^E = \int_{-\infty}^{E} [K_\epsilon * \mathcal{E}](\lambda) d\lambda, \quad \hat{Q}_\epsilon^E = \mathbb{I} - \hat{P}_\epsilon^E, \tag{6}$$

where $\mathbb{I}$ denotes the identity operator. The convolution $[K_\epsilon * \mathcal{E}]$ is a *bona fide* operator-valued function, and so the above definition makes sense. Finally, we define

$$\hat{x}_\epsilon^E = \hat{Q}_\epsilon^E \hat{x} \hat{P}_\epsilon^E, \quad \hat{y}_\epsilon^E = \hat{P}_\epsilon^E \hat{y} \hat{Q}_\epsilon^E,$$

and the smoothed infinite-dimensional local Chern marker on a basis site j up to energy value E as

$$C_j^E = -4\pi \operatorname{Im}\left\{ \langle j | \hat{x}_\epsilon^E \hat{y}_\epsilon^E | j \rangle \right\} / A_c.$$

In the following, we use $\epsilon = 0.05$ and the sixth-order kernel in Appendix A, where we provide algorithmic details.

As an example, the results for the effective Chern marker for infinite size are shown for a square crystalline lattice with a Hamiltonian of Eq. (1) in Fig. 3. The Hofstadter butterfly has no states with a nonzero effective Chern marker, as expected, apart from a handful that have a vanishing Chern marker as the algorithm converges. The algorithm we develop to compute topological properties for infinite-size systems is widely applicable. It can be used to study other quasiperiodic, aperiodic, or even perturbed periodic lattices with complex structure.

B. Locality measures

To characterize the prevalence of a state throughout the entire lattice, it is necessary to use locality measures. One of the most common locality measures is the inverse participation ratio of the nth eigenstate,

$$\mathrm{IPR}^n = \sum_j^N \left| \psi_j^n \right|^4, \tag{7}$$

where ψ_j^n is the wave function of the nth eigenstate at site j and $0 \leqslant \mathrm{IPR}^n \leqslant 1$. For a state that is extended across the entire lattice, IPR^n will be close to zero. Otherwise, if the state is strictly localized to a single site or a collection of sites, IPR^n will be approximately 1. The use of IPR^n alone will not characterize whether or not we have a BLT state or ES. While the IPR^n of ESs will typically fluctuate around a fixed value, the IPR^n of BLT states will vary, making the distinction between certain BLT states and ESs difficult. To make the distinction between ESs and BLT states much more clear, we will also make use of a radial measure, which we define as

$$\mathcal{L}^n = {N_f}^{-1} \sum_j \rho_j^n r_j, \tag{8}$$

where $\rho_j^n = |\psi_j^n|^2 / \max(|\psi^n|^2)$ is the rescaled probability density if this quantity is at least $0.75\max(|\psi^n|^2)$, and $\rho_j^n = 0$ otherwise. Here, N_f is the number of elements for which $\rho_j^n > 0$, and r_j is the jth site normalized radial coordinate with $0 \leqslant r_j \leqslant 1$. $\mathcal{L}^n$ is defined such that for every state $0 \leqslant \mathcal{L}^n \leqslant 1$, with ESs having $\mathcal{L}^n \sim 1$ and BLT states $\mathcal{L}^n < 1$. The radial measure then gives the degree to which the overall density profile is localized towards the lattice center, whereas IPR^n tells us whether or not the state is strictly localized to a subset of lattice sites. Note that, for regular bulk states, we also have $\mathcal{L}^n < 1$. However, we distinguish between bulk states and in-gap BLT states via the above topological measures.

C. Transport properties

The most significant physics of in-gap states are their transport properties. For ESs, transport is supported along the edge of the system. The BLT states characterized in this paper support transport along localized regions within the bulk of the lattice. For the finite lattice, this requires the evolution of the current state $\psi(t_0)$ under the time evolution such that the final state is $\psi(t_1) = e^{-iH(t_1 - t_0)} \psi(t_0)$. We use a Trotter decomposition of the evolution unitary into discrete time steps in our calculations. Our Hamiltonian is always time-independent, and we do not drive the system in any way.

For the infinite-size lattice, we cannot just apply the time evolution to a finite truncation, since we want to avoid finite-size effects. For a holomorphic function g, Cauchy's integral formula yields

$$g(H) = \frac{1}{2\pi i} \int_\gamma g(z)(H - z)^{-1} dz, \tag{9}$$

where γ is a closed contour looping once around the spectrum. Transport properties are computed via the choice $g(z) = \exp(-izt)$. The contour integral is computed using quadrature and approximations of the resolvent $(H - z)^{-1}$ via rectangular truncations as above. In particular, the rectangular truncation of the Hamiltonian is chosen adaptively through *a posteriori* error bounds. This allows us to perform rigorous computations with error control that are guaranteed to be free from finite-size or truncation/discretization effects, directly probing the transport properties of the infinite lattice. This is difficult to achieve via other methods such as truncating the tile since it can be difficult to predict how large the truncation needs to be *a priori* [an example for the AB tiling is given in Ref. [97] (Sec. 6.1)].

IV. BULK LOCALIZED TRANSPORT STATES

For the Hamiltonian Eq. (1) on a crystalline lattice with open boundary conditions, there are generally two types of states—ordinary bulk states and in-gap ESs. This is all that would usually be expected without the presence of perturbations or defects. Perturbations could include, for example, the introduction of impurities, which can have in-gap states bound to them [13,50–54], or the presence of internal hard edges, as in fractal lattices [47–49].

In this section, we show that quasicrystals in the presence of a magnetic field possess a third kind of state—*BLT states*. Examples of all three possible states, i.e., a bulk state, an ES state, and a BLT state, are shown in Fig. 4 for a finite-size AB tiling vertex model with 1273 sites, along with their corresponding local Chern markers. In the figures throughout this paper, we saturate the color maps of the local Chern marker distributions to a range that shows the variation within the bulk. This is necessary because of large divergences in the local Chern marker near edges of the system, which occur so that the sum of all local Chern markers in a given state will be

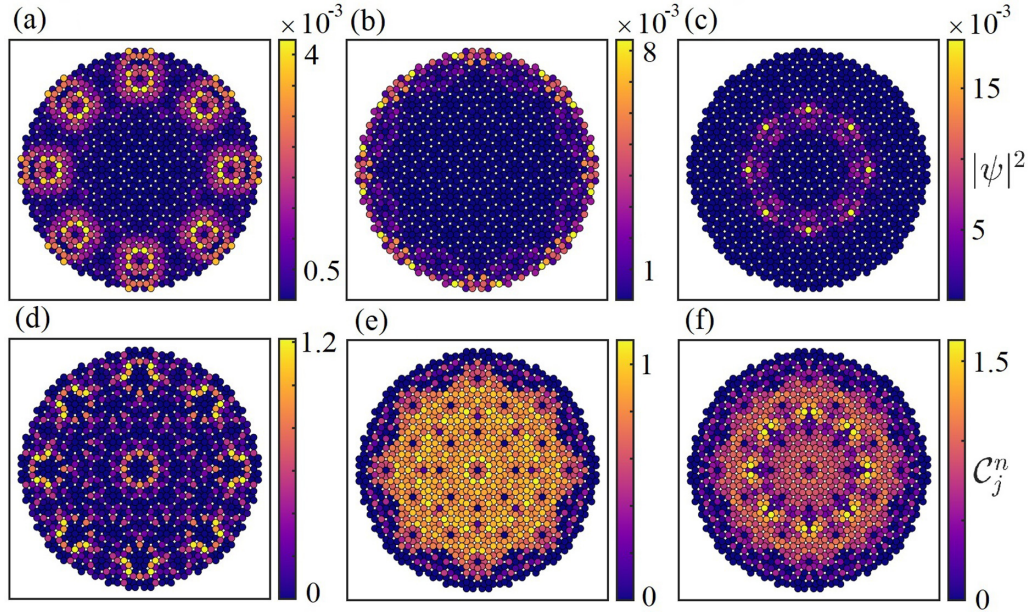

FIG. 4. Example states (a)–(c) and their $\mathcal{C}_j^n$ distributions (d)–(f), showing (a), (d) a normal bulk eigenstate at $n = 300$; (b), (e) an ES at $n = 485$; and (c), (f) a BLT state at $n = 491$. For each case, the corresponding Bott indices are (a) $\mathcal{B} = 0$, (b) $\mathcal{B} = 1$, and (c) $\mathcal{B} = 1$. The $\mathcal{C}_i^n$ distributions have the minimum value saturated to 0 for visual clarity.

zero [38,82]. In the bulk of the lattice, these fluctuations are generally small, allowing the effective Chern marker of a state to be visualized under a suitable range for the color map.

It is worth mentioning that BLT states have not been observed in quasicrystals composed of single tiles, such as the Rauzy tiling [38]. The Rauzy tiling is an example of a quasicrystal that would not be expected to host BLT states, due to the lack of a magnetic aperiodicity.

A. Scaling of the in-gap states

Using the radial measure of Eq. (8), combined with the effective Chern marker of the state, we split our spectra into ES, BLT state, and bulk state components. Figure 5 shows the variation in the number of ESs or BLT states as we vary the flux for different finite system sizes. There is also a characteristic dip in the in-gap states at a single flux within $0 \leqslant \phi/\phi_0 \leqslant 1$, as is the case for ESs in a crystalline lattice.

Interestingly, the number of BLT states as a proportion of the total number of states is increasing with system size. This contrasts with ESs in the gap, whose proportion decreases with system size (due to the bulk increasing in size faster than the edge). By considering larger system sizes for the finite system in Fig. 6, we show that, as expected, the proportion of ESs tends towards zero. However, the proportion of BLT states increases with system size and appears to converge towards a nonzero number. In fact, the values near convergence are ∼20–40 % of the total states, which is considerable and seen across a broad range of flux values.

B. A zoo of BLT states

There is a rich and varied *zoo of BLT states* for the AB vertex model in a magnetic field, for both finite and infinite

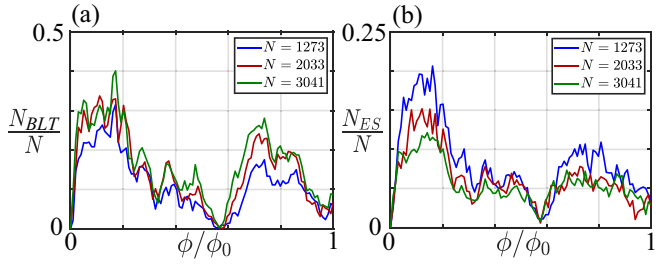

FIG. 5. Number of in-gap states as a function of flux, showing (a) the number of BLT states (N_{BLT}) and (b) the number of ESs (N_{ES}). The blue, red, and green curves correspond to $N = 1273$, 2033, and 3041 lattice sites, respectively. Generally speaking, ESs usually decrease in presence for the larger system sizes, as we expect. However, the number of BLT states may actually increase in some intervals of flux values.

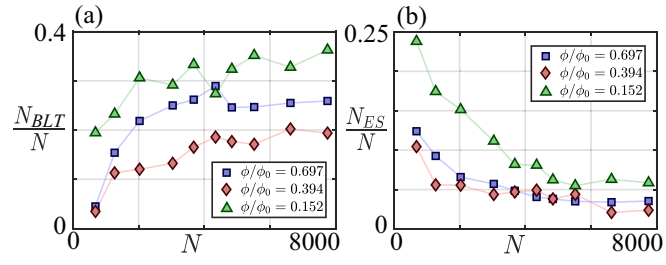

FIG. 6. Number of in-gap states as a function of system size, showing (a) the number of BLT states (N_{BLT}) and (b) the number of ESs (N_{ES}). The blue squares, red diamonds, and green triangles correspond to a ϕ/ϕ_0 of 0.697, 0.394, and 0.152, respectively. For each flux, there are signs of overall convergence at large N for the total number of different topological states, but fluctuations can frequently occur due to the inhomogeneous nature of the lattice.

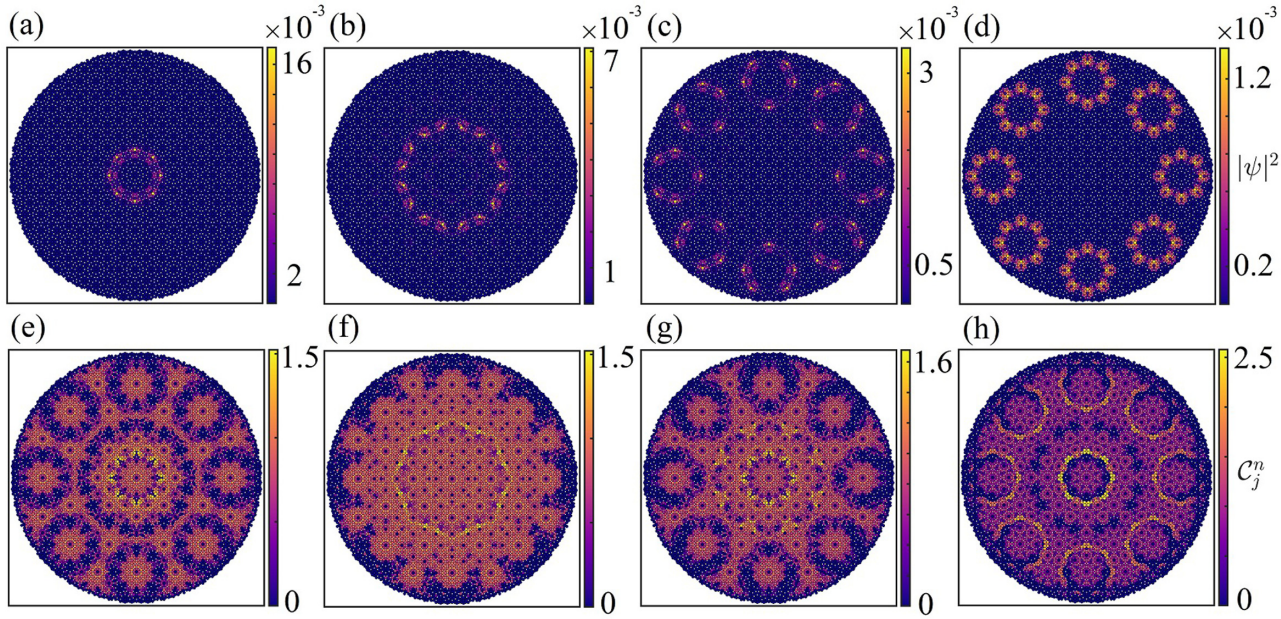

FIG. 7. Example BLT states (a)–(d) and their $\mathcal{C}_j^n$ distributions (e)–(h) for a larger portion of the AB tiling with 7753 sites. Each state corresponds to (a), (e) $n = 3022$; (b), (f) $n = 2987$; (c), (g) $n = 3030$; and (d), (h) $n = 2219$.

systems. The BLT states are also prevalent in a variety of other quasicrystals—see Appendix B.

We first fix the flux to $\phi/\phi_0 = 0.69$ and give examples of the varied structure of BLT states in Fig. 7. To find the large variety of BLT states realizable at this flux, we simply need to extend the system size from the previous consideration in Fig. 4. The examples shown in Fig. 7 are for 7753 sites. Not only is the original BLT state from Fig. 4(c) retained in Fig. 7(a), but we also realize BLT states in different regions of the lattice, both far into the bulk and nearer the boundary of the system. The form of the states in Fig. 7 further explains the trend of the proportion of BLT states shown in Fig. 6 as we increase the system size. As the quasicrystal becomes larger, there are more regions of the lattice to which the BLT states can localize. We also show the local Chern markers for each state in Fig. 7, where it can be seen that the effective Chern marker of the bulk is nonzero, as the majority of sites in the bulk have a nonzero local Chern marker.

BLT states are not a peculiarity of a single flux, and we show a range of example BLT states at different flux in Fig. 8. All the states shown in Fig. 8 have a nonzero Bott index and effective Chern marker. It is clear from the examples of Fig. 8 that the BLT states are not an artefact of a single region or a subset of regions of the lattice. Instead, they appear throughout the system, with their location dependent on the flux. This hints that their origins are due to an interplay of the constant magnetic field with the quasiperiodicity of the lattice, which we explore further in Appendix C. The appearance of BLT states is as diverse as the usual bulk states observed for the quasicrystal, reflecting the quasiperiodic nature of the system. Figures 8(d) and 8(e) show examples that have localization to a single site, rotationally symmetric sets of single sites, or intricate localized structures. A key property of the BLT states appears to be their ability to appear in many regions of the quasicrystalline lattice. This ability could prove useful in future applications, as their position is not restricted and could be tuned without altering the lattice geometry.

A truly intriguing question for BLT states is whether they survive in the infinite-size system. We confirm that the BLT states can indeed exist in the infinite-size quasicrystal by applying the method of Secs. II B and III A 2. A set of example states are shown in Fig. 9, all with a nonzero effective Chern marker. The similarity of these BLT states to the finite-size results already discussed is striking. Again, the region where BLT states localize is flux-dependent. The persistence of BLT states for the infinite-size quasicrystal is an important contrast with the edge states of Hamiltonian (1). In crystalline systems, we would expect all states in the infinite size to be in the bulk bands, with no in-gap states. However, with the BLT states preserved, a quasicrystal in a magnetic field can have states with properties that are usually considered to be related to being in-gap, even for the infinite-size lattice without defects or boundaries.

C. Prevalence of the BLT states

The periodic fractal nature of the Hofstadter butterfly is not preserved for quasicrystalline systems. For quasicrystals, the energy-flux plane still contains a rich structure, which is now, in general, also aperiodic. The structure of the energy-flux plane for quasicrystals has been previously studied [37,43], and will now be utilized to show the prevalence of BLT states throughout the single-particle "phase diagram" of Hamiltonian (1).

In Figs. 10(a)–10(d), we show the finite-size Hofstadter butterfly for two lattice sizes, with the color map being the effective Chern marker $\mathcal{C}^n$ for each state and the corresponding radial measure of Eq. (8) for every in-gap state (i.e., nonzero $\mathcal{C}^n$). As a reminder, the effective Chern marker is calculated from the integer of maximal counts in the

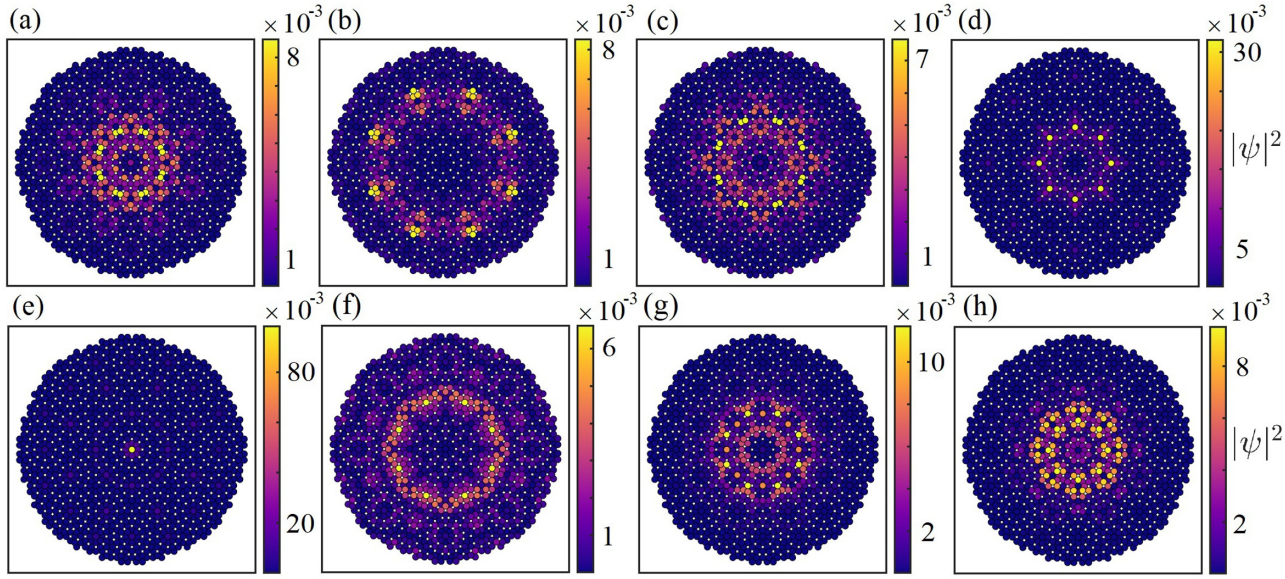

FIG. 8. Example BLT states at different flux. Each state corresponds to (a) $n = 290$ at $\phi = 0.141\phi_0$, (b) $n = 379$ at $\phi = 0.394\phi_0$, (c) $n = 582$ at $\phi = 0.546\phi_0$, (d) $n = 90$ at $\phi = 0.909\phi_0$, (e) $n = 98$ at $\phi = 0.909\phi_0$, (f) $n = 291$ at $\phi = 1.250\phi_0$, (g) $n = 135$ at $\phi = 1.579\phi_0$, and (h) $n = 309$ at $\phi = 2.623\phi_0$. For each case, the corresponding Bott indices are (a) $\mathcal{B} = -2$, (b) $\mathcal{B} = -1$, (c) $\mathcal{B} = -1$, (d) $\mathcal{B} = 1$, (e) $\mathcal{B} = 1$, (f) $\mathcal{B} = -1$, (g) $\mathcal{B} = 1$, and (h) $\mathcal{B} = 1$, meaning each state shown is in-gap.

distribution of local Chern markers for a given state. From this, we can see that there is a significant number of states that are in-gap and within the bulk, i.e., with $\mathcal{L}^n < 1$ and $\mathcal{C}^n \neq 0$. The inverse participation ratio IPR^n for BLT states is also plotted in Figs. 10(e) and 10(f), which reveals that the majority of BLT states are not strictly localized to a small subset of lattice sites. The locality and extent of BLT states is an interesting question, and one we consider further in Appendix D. We also show the energy-flux plane for the infinite-size quasicrystal in Fig. 11. In this scenario, we compute effective Chern markers using the algorithm outlined in Appendix A 2 across a full range of energy values for Fig. 11(a). To retain states that belong to the infinite size and remove spectral pollution/ESs, we also use Algorithm 1 to restrict the energy to values within the infinite size in Fig. 11(b) up to a specified error bound of 0.01. BLT states are then present for the infinite system

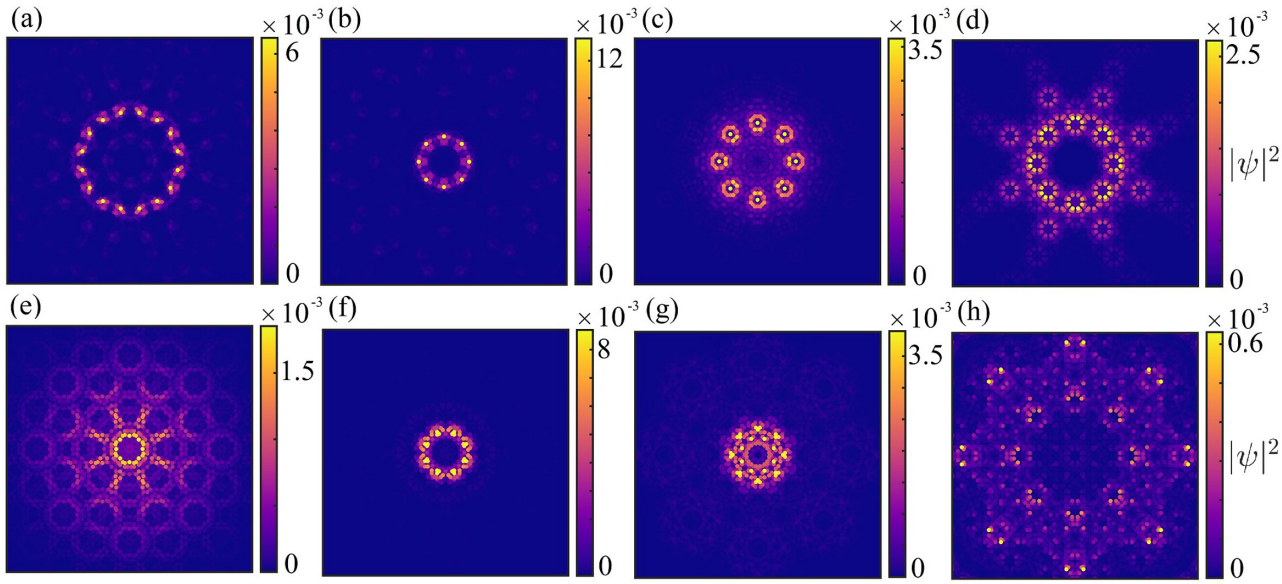

FIG. 9. Density profiles of example BLT states on the infinite tiling for (a), (b) $\phi = 0.69\phi_0$; (c) $\phi = 0.2\phi_0$; (d), (e) $\phi = 0.4\phi_0$; (f) $\phi = 0.8\phi_0$; and (g), (h) $\phi = 0.1\phi_0$. Each state corresponds to an energy value (with shown error bounds) of (a) $E = -0.987\,30 \pm 3 \times 10^{-5}$ J, (b) $E = -0.974\,79 \pm 2 \times 10^{-5}$ J, (c) $E = -0.977\,43 \pm 2 \times 10^{-5}$ J, (d) $E = -1.562\,934 \pm 8 \times 10^{-6}$ J, (e) $E = -0.788\,55 \pm 2 \times 10^{-5}$ J, (f) $E = -0.997\,183 \pm 5 \times 10^{-6}$ J, (g) $E = -1.604\,22 \pm 2 \times 10^{-5}$ J, and (h) $E = -1.5002 \pm 3 \times 10^{-4}$ J. All states shown have a nonzero effective Chern marker, and they are therefore BLT states with in-gap characteristics.

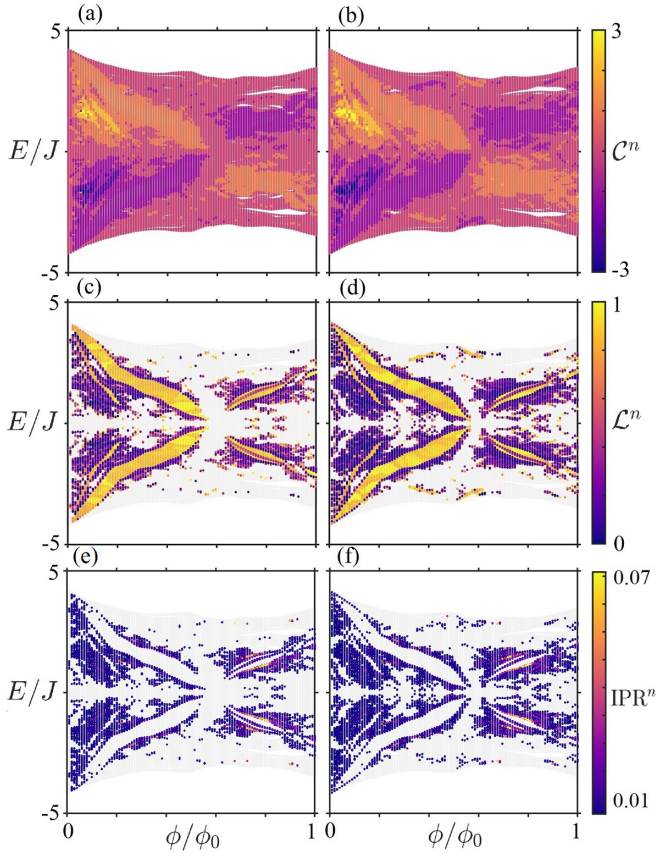

FIG. 10. Spectra of the quasicrystalline lattice, where each state is labeled according to either their (a), (b) effective Chern marker $\mathcal{C}^n$; (c), (d) radial measure $\mathcal{L}^n$, or (e), (f) the inverse participation ratio IPR^n. Each column considers (a), (c), (e) $N = 1273$ and (b), (d), (f) $N = 3041$ sites. In (b), (d), we only plot the $\mathcal{L}^n$ of in-gap states, with other states plotted in light translucent gray. In (e), (f), we only plot the IPR^n of BLT states. In-gap states can be observed throughout the spectra, and they become more prominent for the larger system size.

through large ranges of flux, with states possessing a nonzero effective Chern marker, even after ESs are removed from the system. The regions where BLT states are present in the infinite-size quasicrystal map well to those present in the finite size.

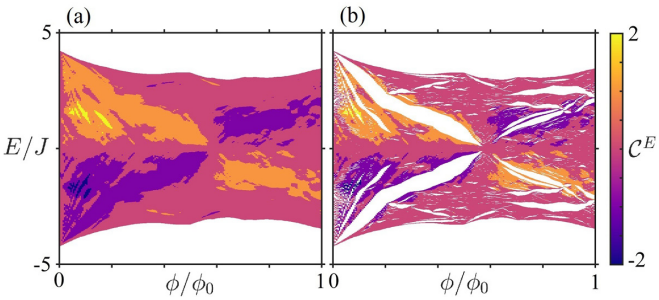

FIG. 11. Effective Chern markers for the infinite AB tiling, showing (a) the effective $\mathcal{C}^E$ over a range of energy values E and (b) a restricted range over values in the spectrum of the infinite lattice up to the specified tolerance 0.01. States in (b) with $\mathcal{C}^E \neq 0$ correspond to BLT states.

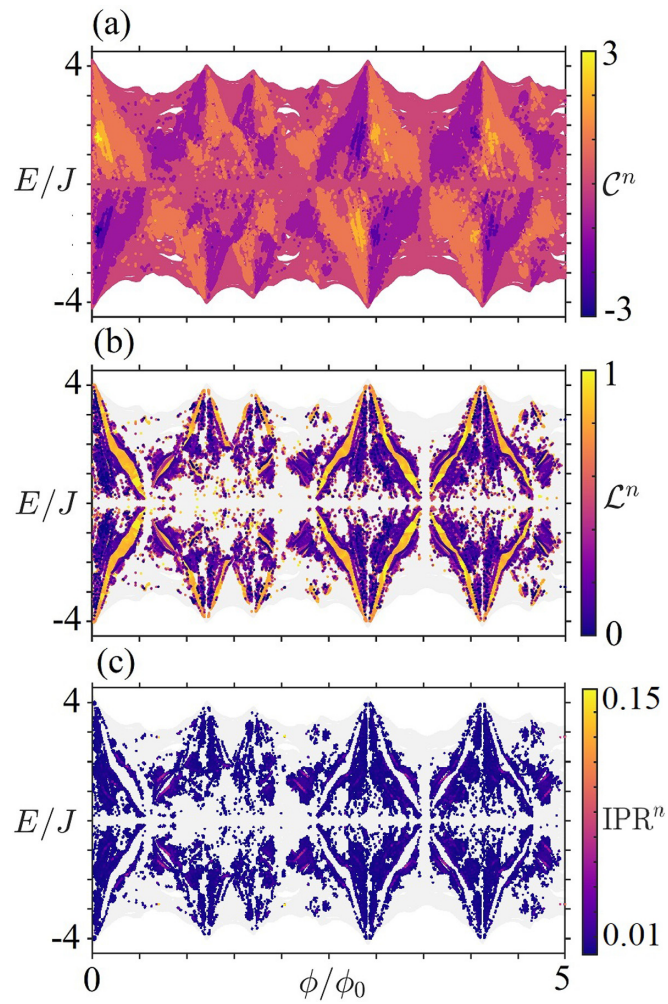

FIG. 12. Spectra of the quasicrystalline lattice, where each state is labeled according to either (a) the effective Chern marker $\mathcal{C}^n$, (b) the radial measure $\mathcal{L}^n$, or (c) the inverse participation ratio IPR^n across a larger range of ϕ/ϕ_0 for $N = 1273$. In (b) and (c), we again only plot either in-gap states or BLT states, respectively, as per Fig. 10. As expected, the Hofstadter butterfly is aperiodic and has a rich internal structure, with many different regions hosting BLT states.

The aperiodic Hofstadter butterflies in both the finite and infinite size show that BLT states are not a single set of peculiar states limited to the examples shown in the previous section. Instead, BLT states are present in the majority of parameter space for Hamiltonian Eq. (1), with BLT states even dominating the spectrum for particular ranges of the flux. We can go to larger values of the flux, as shown in Fig. 12, and observe even more BLT states. The prevalence of BLT states and their variety could make the utilization of their supported BLT (discussed in Sec. V) particularly interesting.

D. Different finite patches

So far, we have explored the formation of BLT states in a quasiperiodic tiling with perfect rotational symmetry. We now explore the infinite-size spectra for AB tilings that no longer contain the central symmetry point, and we show that

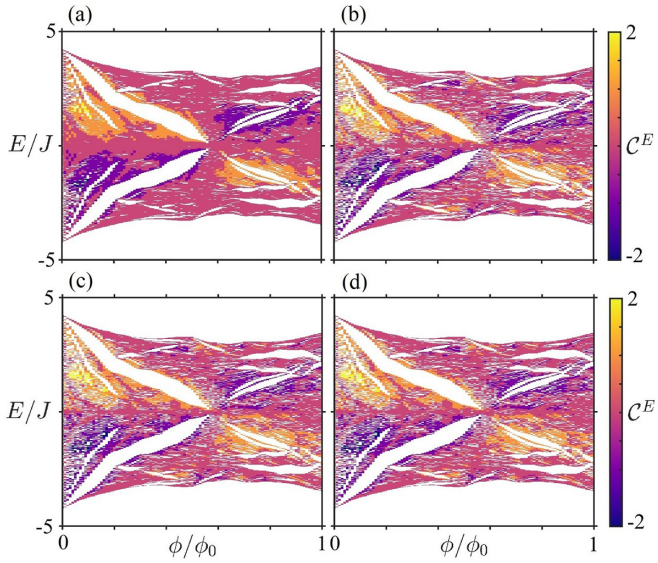

FIG. 13. Effective Chern markers $\mathcal{C}^E$ over a restricted energy range of the infinite lattice for AB tilings with offset vectors of (a) $\vec{r} = [0, 0]l$ (rotationally symmetric tiling), (b) $\vec{r} = [63.82, 43.92]l$, (c) $\vec{r} = [128.35, 71.06]l$, and (d) $\vec{r} = [400.11, 183.22]l$, where l is the quasicrystalline bond length. States with $\mathcal{C}^E \neq 0$ correspond to BLT states.

BLT states still form in the absence of rotational symmetry. To construct these tilings, we simply set the origin of the tiling to some generic offset vector $\vec{r}$, and we construct the finite patch around this point. In Fig. 13, we plot several examples of the infinite-size spectra for a variety of offset vectors $\vec{r}$, including the case of $\vec{r} = [0, 0]$, which corresponds to the rotationally symmetric results in Fig. 11(b) as a reference. For these considered cases, we observe that all of the Hofstadter butterflies are almost identical in structure, including the domains in which BLT states are stabilized. The most notable differences are subtle changes in the appearance of gaps in certain intervals and the presence of additional BLT states around $E/J \approx \pm 3.5$ and $\phi/\phi_0 \approx 0.5$, similar to Figs. 10(c) and 10(d).

These results clearly demonstrate that the formation of BLT states is not dependent on the underlying rotational symmetry of the quasicrystal. To better illustrate this, we also plot several examples of BLT states for the offset tilings in Fig. 14, when $\phi/\phi_0 = 0.69$. The states in each of the columns are similar in structure to those within Figs. 9(a) and 9(b), but now with enhanced localization due to the broken rotational symmetry. Furthermore, the difference of energies between the states observed in the offset tilings and the states in Figs. 9(a) and 9(b) are small, meaning that they are almost degenerate. Nearly degenerate BLT states should be expected in quasicrystals due to the self-similar regions that can occur. Note that the states are nearly degenerate instead of degenerate due to the quasicrystalline nature of the system, i.e., the tails of the localized BLT states will extend into different regions of the lattice, and as it is not crystalline this will result in small offsets in energy. In principle, for an arbitrarily large quasicrystal it is possible for two nearly degenerate BLT states to have an arbitrarily small energy difference, but this has yet to be observed.

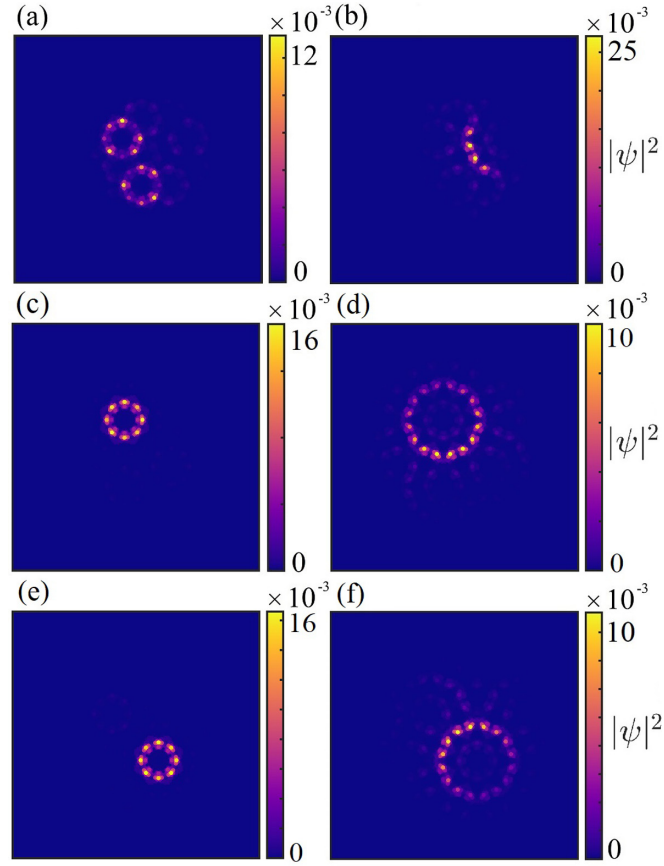

FIG. 14. Density profiles of example BLT states on the infinite-size offset tilings for $\phi = 0.69\phi_0$, with offset vectors (a), (b) $\vec{r} = [63.82, 43.92]l$; (c), (d) $\vec{r} = [128.35, 71.06]l$; and (e), (f) $\vec{r} = [400.11, 183.22]l$, where l is the quasicrystalline bond length. Each state has an energy of (a) $E = -0.9752 \pm 4 \times 10^{-4}$ J, (b) $E = -0.9865 \pm 5 \times 10^{-4}$ J, (c) $E = -0.9750 \pm 2 \times 10^{-4}$ J, (d) $E = -0.9873 \pm 3 \times 10^{-4}$ J, (e) $E = -0.9750 \pm 2 \times 10^{-4}$ J, and (f) $E = -0.9872 \pm 3 \times 10^{-4}$ J. The states in columns (a), (c), (e) and (b), (d), (f) are almost degenerate with the two states in Figs. 9(b) and 9(a), respectively.

V. BULK LOCALIZED TRANSPORT

One of the most interesting properties of in-gap topological states is their support of transport. For crystalline lattices in constant magnetic fields, this is usually considered by launching a state (or particle) along the edge of the system, and observing the robust transport of a component of the state around the boundaries. If a boundary is instead formed within the lattice, e.g., between a topological and nontopological region, then transport can also be supported along such features due to the presence of in-gap states bound to the interface.

The BLT states found in this work are another type of in-gap state. Therefore, we expect them to support transport along their locality. Indeed, we find that a quasicrystal in a magnetic field can also support long-lived BLT within the bulk, as depicted in Fig. 1, due to the presence of BLT states. Several examples of BLT are shown for both the finite and infinite size in Figs. 15 and 16, respectively, for the AB tiling. It is clear that a component of the initial state populates the BLT state, allowing for BLT to be supported. Note, here, that

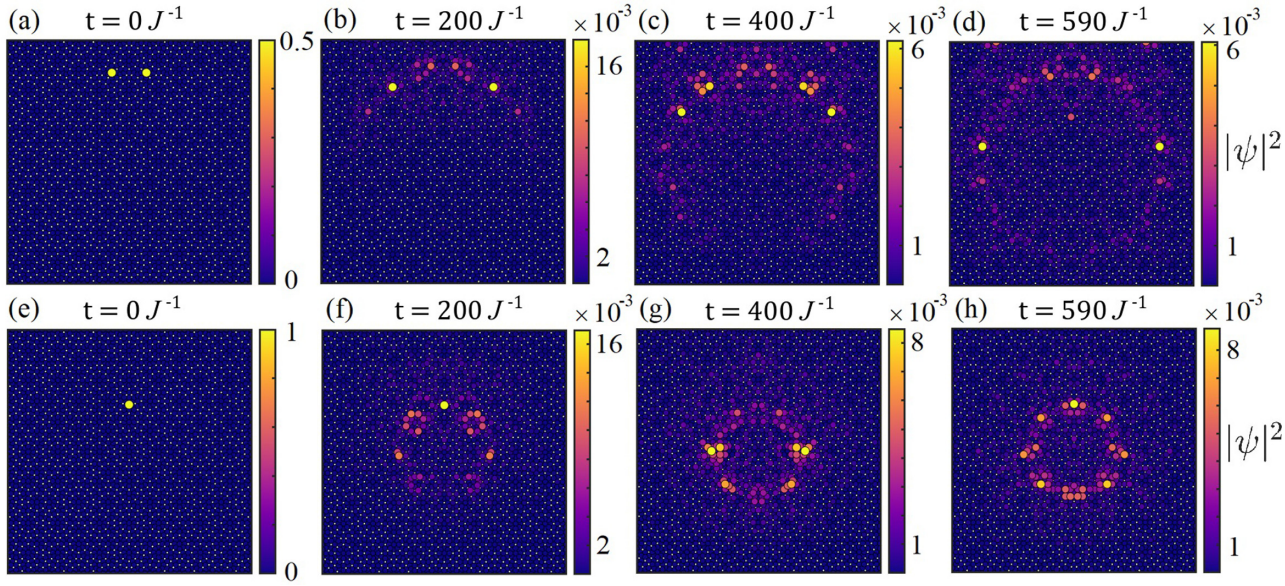

FIG. 15. Dynamical transport due to the presence of BLT states, showing the evolution of (a)–(d) state $n = 2987$ and (e)–(h) state $n = 3022$ on the larger lattice of 7753 sites. Each column corresponds to a time frame of (a), (e) $t = 0$ J^{-1}; (b), (f) $t = 200$ J^{-1}; (c), (g) $t = 400$ J^{-1}; and (d), (h) $t = 590$ J^{-1}. Our Hamiltonian is always time-independent, and we do not drive the system in any way.

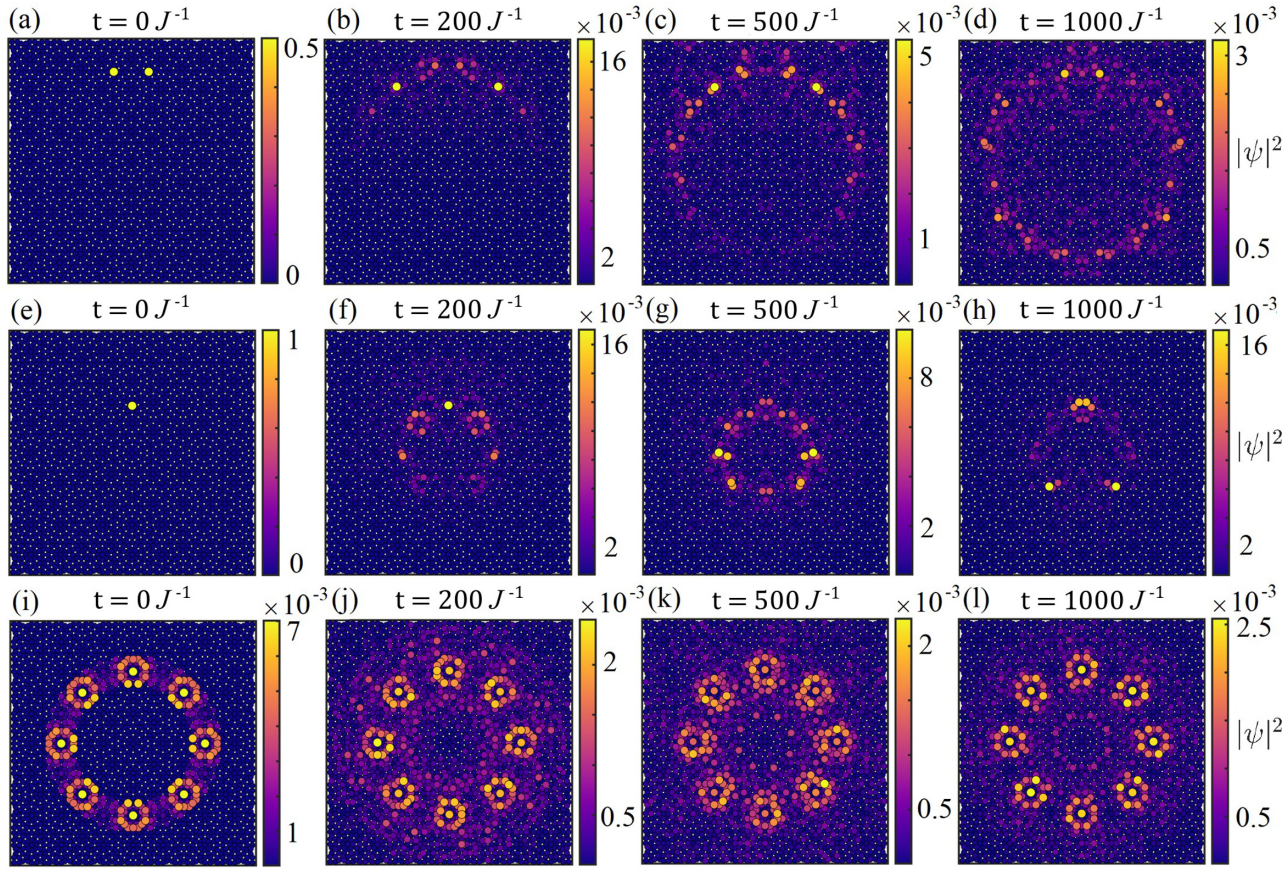

FIG. 16. Infinite-size dynamical transport due to the presence of BLT states, at time $t = 0$ J^{-1} (first column), $t = 200$ J^{-1} (second column), $t = 500$ J^{-1} (third column), and $t = 1000$ J^{-1} (fourth column). The first two rows correspond to the BLT states in Fig. 15 ($\phi = 0.69\phi_0$), but now computed on the full infinite tiling. The third row corresponds to an excitation of the BLT state at $\phi = 0.2\phi_0$ in Fig. 9(c). Our Hamiltonian is always time-independent and we do not drive the system in any way.

we do not attempt to load into the BLT states, meaning we lose population into the other states that overlap with the initial state. For experimental scenarios, it would be prudent instead to use state preparation methods to load into the BLT states [98–100].

The transport shown for the infinite-size lattice in Fig. 16 is remarkable. For the infinite size, the usual transport along the edge is not present due to the lack of said edge. For the periodic infinite size, we can still have transport carrying states due to the presence of an interface or impurities. However, in the quasicrystal, an interplay of the magnetic field and quasiperiodicity can localize the particle to the bulk in the infinite size without any alterations to the lattice. These infinite-size states are then as capable of carrying transport along them as any edge state in the finite system.

A key property of BLT could be the possibility of using its varied location throughout the lattice itself. In a crystalline finite system, the transport is only along the edge, or any internal edges imposed by the lattice structure and/or defects. However, with BLT we have shown that it is possible to have transport supported in multiple locations within the lattice for any given flux. By varying the flux, we can also tune where the BLT is supported. BLT can then give a degree of control for transport to occur within the bulk. By showing that this can be done in the infinite size, we have shown that BLT is independent of the size of the lattice, or the exact form of the boundary. This is in stark contrast to in-gap ESs, whose presence can in some cases be entirely reliant on the geometry of the edge [101].

VI. DISCUSSION AND CONCLUSIONS

We have shown that the conventional picture of insulators, metals, and topological insulators with surface states is not the full story for quasiperiodic systems. When the quasiperiodic nature of a quasicrystalline lattice interacts with a magnetic field, it is possible for states to form that are unique in their character. These states are localized to the bulk, but are in-gap and support transport along them in the bulk. The BLT states are far from a peculiarity and can exist throughout the spectra of 2D quasicrystals in magnetic fields due to a magnetic aperiodicity. Magnetic aperiodicity is not an artificial construct and is natural in the majority of 2D quasicrystals, due to the incommensurate nature of the building blocks of the lattice. For the case of the vertex models studied in this work, this incommensurate nature arises from the incommensurate areas of the prototiles. Sometimes, BLT states are even the dominant in-gap state for large finite system sizes. We confirmed that BLT states can exist in a variety of regions within the bulk of the lattice, with their position being dependent on the flux, or equivalently the magnetic field strength. Through the use of a new numerical technique, we have also shown that BLT states are present in the infinite-size lattice. This is quite remarkable as they are in-gap states, with corresponding nonzero topological measures. Through considering different finite patches of infinite size quasicrystals, we have observed that nearly degenerate BLT states can occur over large separations in space due to the self-similarity of the quasicrystals studied. Finally, by exciting regions within the bulk of the lattice, we have shown that BLT is supported in both finite- and infinite-size lattices.

Potential experimental realization: While there are current developments of realizing quasicrystalline problems in cold atoms [29,32], a promising setting for current realization of the BLT states could be photonic lattices [102]. Photonic lattices allow a high degree of controllability in the lattice geometry and are favorable for realizing the BLT states due to a large number of sites being possible. The lattice is usually etched into the two-dimensional plane of a fused silica crystal, with time being transposed onto the third dimension of the crystal. Photonic lattices are good simulators for single-particle physics, and synthetic gauge fields can be realized via helical waveguides [103], a Floquet steplike approach [22,104], or a strain across the lattice [105]. Furthermore, there has been a recent proposal to realize a Penrose quasicrystal in a synthetic vector potential using helical waveguides [35]. As the key to the realization of BLT states is the magnetic aperiodicity, we expect that any of these current techniques could potentially be utilized to probe the physics of BLT states.

Open problems and future research directions: One possible line of work is to consider the nature of the spectra for the infinite-size tiling. Usually, we would consider these states to all be ordinary bulk states, but, as we have shown, this is not necessarily the case, even without any impurities or long-range disorder in the system. Another interesting question is how the BLT states would appear or alter the physics in the presence of interactions. The study of the physics of two-dimensional quasicrystals including interactions is an emerging topic [106–108]. With the recent advances in many-body numerical techniques [109–111], the physics of BLT states and their ramifications in quasicrystalline lattices in the many-body regime could soon be probed.

The reliance on magnetic aperiodicity also initiates an interesting set of questions. Magnetic aperiodicity is not a sole property of quasicrystals and could be incorporated into crystal structures by deformations like that considered briefly in Appendix C. This approach could be used to design effective regions in the system where BLT states are desired to localize, through the appearance of magnetic aperiodicity. These regions could then be tuned to support or not support transport through changes in the applied magnetic field strength. This would potentially allow the design and control of specific regions supporting localized transport within a crystalline lattice bulk by introducing quasicrystalline-like deformations.

Final remarks: The understanding of electronic-like states in quasicrystals is at an early stage of development, especially concerning potential applications to quantum technologies. There is much work to be done to realize the potential of these fascinating and complex structures. This work has shown one possible exotic behavior of these systems in magnetic fields—the existence of BLT states and their supported transport. Future work to understand the applications of BLT states to quantum problems, like the applications considered for typical edge states [3,6,112,113], could be particularly fruitful.

The data for all results shown in this manuscript is available in open access at [114]

ACKNOWLEDGMENTS

The authors acknowledge helpful discussions with Andrew J. Daley, Terry A. Loring, Manuel Valiente, and Alexander Watson. D.J. acknowledges support from EPSRC CM-CDT Grant No. EP/L015110/1. M.J.C. acknowledges support from a Research Fellowship at Trinity College, Cambridge, and a Fondation Sciences Mathématiques de Paris Postdoctoral Fellowship at École Normale Supérieure. A.E.B.N. and C.W.D. acknowledge support from the Independent Research Fund Denmark under Grant No. 8049-00074B. C.W.D. acknowledges support by the EPSRC Programme Grant DesOEQ (EP/P009565/1), the European Union's Horizon 2020 research and innovation program under grant agreement No. 817482 PASQuanS, and the EPSRC Quantum Technologies Hub for Quantum Computing and Simulation (EP/T001062/1).

APPENDIX A: DETAILS OF THE INFINITE-SIZE ALGORITHMS

This Appendix provides details of the algorithms used to tackle infinite-dimensional spectral problems. Dealing with infinite dimensions is more subtle than finite dimensions, and not every computational spectral problem can be solved [115]. We split the discussion into three subsections corresponding to each computed spectral quantity.

1. Computing spectra with error control

We describe the algorithm for infinite, sparse (finitely many nonzero entries in each column) matrices representing Hermitian Hamiltonians. For nonsparse matrices and even non-Hermitian operators, see [59]. Extensions to unbounded operators and partial differential operators can be found in [75].

In our setting, the Hamiltonian H can be represented by an infinite Hermitian matrix, $\hat{H} = \{\hat{H}_{ij}\}_{i,j\in\mathbb{N}}$. We are given a function $f : \mathbb{N} \to \mathbb{N}$ such that $\hat{H}_{ij} = 0$ if $i > f(j)$, thus describing the sparsity of $\hat{H}$. For $z \in \mathbb{R}$, the key quantity to compute is

$$F_n(z) := \sigma_{\inf}(P_{f(n)}(\hat{H} - z)P_n),$$

where P_m denotes the orthogonal projection onto the linear span of the first m basis vectors, and $\sigma_{\inf}$ denotes the smallest singular value of the corresponding rectangular matrix. The function F is an upper bound for the distance of z to the spectrum $\mathrm{Sp}(H)$, and it converges down to this distance uniformly on compact sets as $n \to \infty$. There are numerous ways to compute F_n, such as standard iterative algorithms or incomplete Cholesky decomposition of the shifts $P_n(\hat{H} - z)P_{f(n)}(\hat{H} - z)P_n$ (see the supplemental material of [59] for a discussion). The other ingredient is a grid of points $G_n = \{z_1^{(n)}, \ldots, z_{j(n)}^{(n)}\} \subset \mathbb{R}$ providing the wanted resolution r_n over the spectral region of interest.

The algorithm is sketched in Algorithm 1, where $\tilde{F}_n$ denotes the described suitable approximation of F_n (which can be computed in parallel). The simple idea of the method is a local search routine. If $\tilde{F}_n(z) \leqslant 1/2$, we search within a radius $\tilde{F}_n(z)$ around z to minimize the approximated distance to the spectrum. This gives the set M_z which is our best estimate of points in the spectrum near z. The output is then the collection of these local minimizers. The algorithm's output, $\Gamma_n(H)$, converges to the spectrum $\mathrm{Sp}(H)$ of the full infinite-dimensional operator as $n \to \infty$ (for suitable $r_n \to \infty$). Note that this convergence is free from edge states. Moreover, the error bound of the algorithm satisfies

$$\sup_{z\in\Gamma_n(H)} \mathrm{dist}(z, \mathrm{Sp}(H)) \leqslant E_n$$

and the output E_n converges to zero as $n \to \infty$ [59]. For a desired spectral resolution $\delta > 0$, we simply increase n until $E_n \leqslant \delta$. Finally, the output V_n consists of the approximate states corresponding to the output Γ_n.

Algorithm 1. Computation of spectrum and the associated approximate states with error control.

Input: $\hat{H}$, f, n, and G_n (with resolution r_n).

1: For $z \in G_n$, approximate $F_n(z)$ to accuracy $(2r_n)^{-1}$ from above. Call the approximation $\tilde{F}_n(z)$ and assume it takes values in $(2r_n)^{-1}\mathbb{Z}$.

2: For $z \in G_n$, let $v_n(z)$ denote the approximation of the right-singular vector of $P_{f(n)}(\hat{H} - z)P_n$ corresponding to the smallest singular value.

3: For $z \in G_n$, if $\tilde{F}_n(z) \leqslant 1/2$, then set

$$I_z = \{w \in G_n : |w - z| \leqslant \tilde{F}_n(z)\},$$

$$M_z = \left\{w \in I_z : \tilde{F}_n(w) = \min_{x\in I_z} \tilde{F}_n(x)\right\}.$$

Otherwise, set $M_z = \emptyset$.

Output: $\Gamma_n = \cup_{z\in G_n} M_z$ (approximation of spectrum), $E_n = \max_{z\in\Gamma_n} \tilde{F}_n(z)$ (error bound), and $V_n = \cup_{z\in\Gamma_n}\{v_n(z)\}$ (approximate states).

2. Computing spectral measures and local Chern markers

In this section, we assume access to a routine that approximates the action of the resolvent $(H - z)^{-1}$ on a vector with error bounds. In the scenario of the current paper, this can be done through the rectangular truncations $P_{f(n)}(\hat{H} - z)P_n$ and solving the resulting overdetermined linear system in the least-squares sense. The residual converges to zero as $n \to \infty$ and can be used to provide the needed error bounds (Ref. [94], Theorem 2.1).

We use the high-order kernel machinery developed in [95] and set $K_\epsilon(\cdot) = \epsilon^{-1}K(\cdot/\epsilon)$ for a kernel $K \in L^1(\mathbb{R})$. Let $\{a_j\}_{j=1}^m$ be distinct points in the upper half-plane and suppose that the constants $\{\alpha_j\}_{j=1}^m$ satisfy the following (transposed) Vandermonde system:

$$\begin{pmatrix} 1 & \cdots & 1 \\ a_1 & \cdots & a_m \\ \vdots & \ddots & \vdots \\ a_1^{m-1} & \cdots & a_m^{m-1} \end{pmatrix} \begin{pmatrix} \alpha_1 \\ \alpha_2 \\ \vdots \\ \alpha_m \end{pmatrix} = \begin{pmatrix} 1 \\ 0 \\ \vdots \\ 0 \end{pmatrix}. \tag{A1}$$

Then the kernel $K(x) = \frac{1}{2\pi i}\sum_{j=1}^m [\frac{\alpha_j}{x-a_j} - \frac{\overline{\alpha_j}}{x-\overline{a_j}}]$ is an mth-order kernel [95], and we have the following generalization

Algorithm 2. Computation of local Chern markers.

Input: $\hat{H}$, $f, m \in \mathbb{N}$ (order of kernel), $\epsilon > 0$ (smoothing parameter), ΔE (energy or spectral spacing), i (site index), A_c (reference area of the lattice), L [lower bound for $\mathrm{Sp}(H)$] and $M \in \mathbb{N}$ (number of energy values).

1: For $j = 0, 1, \ldots, M$, set $E_j = L + j \times \Delta E$ and

$$\hat{P}^{E_j}_{\epsilon,\Delta E} = \Delta E \sum_{k=0}^{j} \frac{[K_\epsilon * \mathcal{E}](E_{k-1}) + [K_\epsilon * \mathcal{E}](E_k)}{2},$$

where K is an mth-order kernel, and the resolvents $(H - z)^{-1}$ in Eq. (A2) are computed adaptively through rectangular truncations corresponding to the function f.

2: Set $\hat{Q}^{E_j}_{\epsilon,\Delta E} = \mathbb{I} - \hat{P}^{E_j}_{\epsilon,\Delta E}$, with identity operator $\mathbb{I}$.

3: Define the operators

$$\hat{x}^{E_j}_{\epsilon,\Delta E} = \hat{Q}^{E_j}_{\epsilon,\Delta E} \hat{x} \hat{P}^{E_j}_{\epsilon,\Delta E}, \quad \hat{y}^{E_j}_{\epsilon,\Delta E} = \hat{P}^{E_j}_{\epsilon,\Delta E} \hat{y} \hat{Q}^{E}_{\epsilon,\Delta E}.$$

Output: Local Chern markers

$$C_i^{E_j} = \frac{-4\pi}{A_c} \mathrm{Im}\{\langle i | \hat{x}^{E_j}_{\epsilon,\Delta E} \hat{y}^{E_j}_{\epsilon,\Delta E} | i \rangle\}$$

at energy value E_j for $j = 1, \ldots, M$.

of Stone's formula:

$$[K_\epsilon * \mathcal{E}](x) = \frac{-1}{2\pi i} \sum_{j=1}^{m} [\alpha_j (H - (x - \epsilon a_j))^{-1} - \text{c.c.}]. \quad \text{(A2)}$$

Under suitable conditions, mth-order convergence in ϵ holds (i.e., the error scales as ϵ^m up to logarithmic factors). As a natural extension of the Poisson kernel, we consider the choice $a_j = 2j/(m+1) - 1 + i$ for $j = 1, \ldots, m$.

With this in hand, and for a given energy value E, we compute the smoothed spectral projections in Eq. (6) using the trapezoidal rule. The quantities $\hat{x}^E_\epsilon$ and $\hat{y}^E_\epsilon$ can be computed via successive applications of the relevant projectors. This is outlined in Algorithm 2, which computes the local Chern markers over a grid of energy values of spacing ΔE. In practice, the algorithm has two levels of parallelism. We can compute resolvents in parallel across different energy values E_j, and we can perform the algorithm in parallel for different sites indexed by i.

3. Computing transport properties

Finally, we discuss transport properties. For an initial wave function ψ_0, we wish to compute

$$\psi(t) = \exp(-iHt)\psi_0 = \int_\gamma \frac{\exp(-izt)}{2\pi i} [(H - z)^{-1} \psi_0] dz,$$

where γ is a closed contour looping once around the spectrum. Suppose that the spectrum is located in an interval $[a, b] \subset \mathbb{R}$. We take γ to be a rectangular contour split into four line segments: two parallel to the imaginary axis with real parts $a - 1$ and $b + 1$ and two parallel to the real axis with imaginary parts $\pm\eta$ ($\eta > 0$). Along these line segments, we apply Gaussian quadrature with enough quadrature nodes for the desired accuracy (the number of nodes can be found by bounding the analytic integrand). Suppose that the weights and nodes for the quadrature rule applied to the whole of γ are $\{w_j\}_{j=1}^N$ and $\{z_j\}_{j=1}^N$. The approximation of $\exp(-iHt)\psi_0$ is

$$\psi(t) \approx \sum_{j=1}^{N} \frac{w_j}{2\pi i} \exp(-iz_j t)[(H - z_j)^{-1} \psi_0].$$

The vectors $(H - z_j)^{-1}\psi_0$ are computed using the adaptive method outlined in Appendix A 2, which can be performed in parallel across the different quadrature nodes. We also reuse these computed vectors for different times t. Numerically, this requires η to be not too large, and a suitable N can be selected for a finite interval of desired times t.

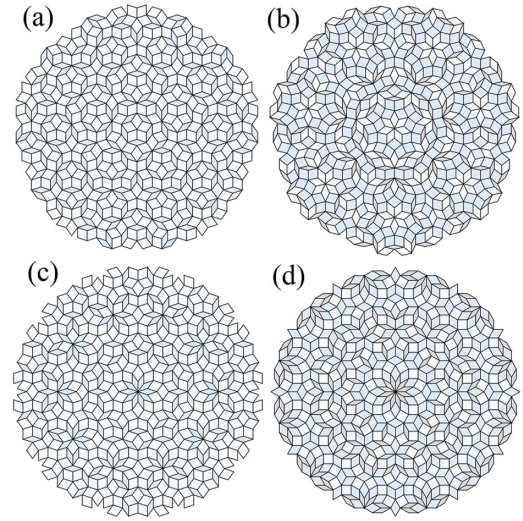

FIG. 17. Finite-size patches of aperiodic rhombic tilings with different rotational symmetries. Here, we consider (a) 5-fold Moore-Penrose tiling, (b) a 7-fold tiling, (c) a 10-fold tiling, and (d) a 12-fold tiling. We show ∼600 sites in the corresponding vertex model for each tiling.

APPENDIX B: BLT STATES IN OTHER QUASICRYSTALS

We have observed that BLT states are prominent within the spectra of the AB vertex model, both with and without a global point of rotational symmetry. We now show that BLT states can also populate the spectra of different kinds of quasicrystals, including ones that possess large defects. As long as a magnetic aperiodicity is retained, BLT states will be preserved.

First, we show this by considering the BLT states present in vertex models of 5-fold, 7-fold, 10-fold, and 12-fold rhombic tilings, which are all deduced from projections of higher-dimensional cubic lattices. Small patches of the tilings are plotted in Fig. 17. The 7-fold and 12-fold lattices now have rhombic tilings with more than two prototiles. As the global rotational symmetry of the rhombic quasicrystal increases, the number of prototiles increases to ensure that no gaps are left in the tiling. The Hamiltonian is still that described by Eq. (1).

Figure 18 plots several example BLT states for each Hofstadter vertex model in the infinite size. This clearly illustrates the appearance of similar looking in-gap states to the ones observed in the eightfold AB tiling. As expected, the structure

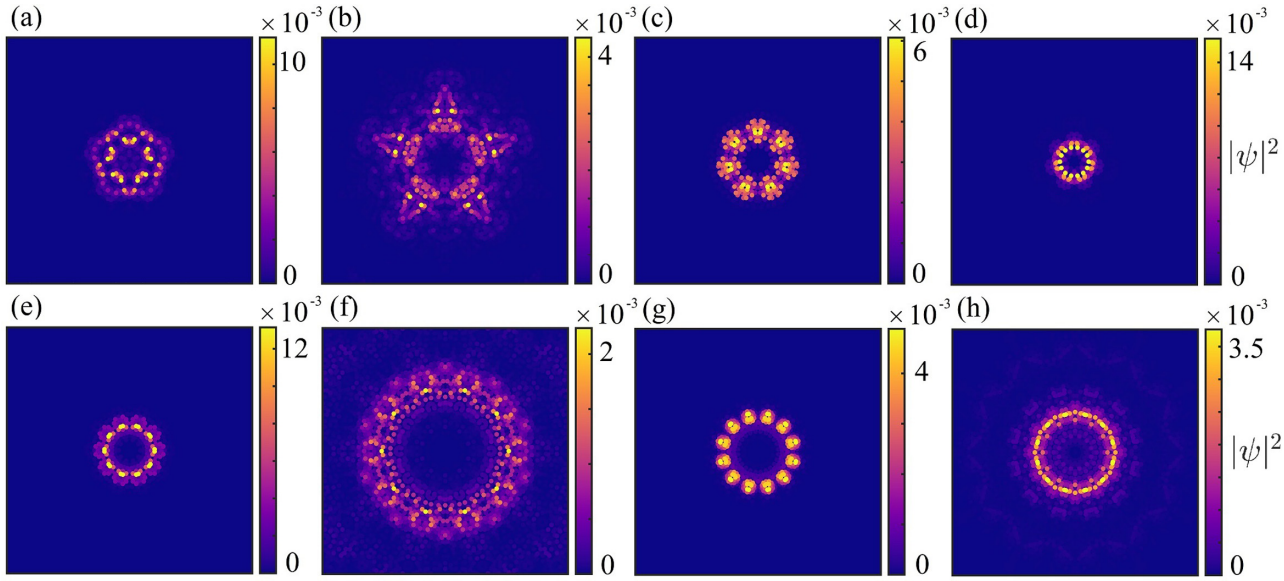

FIG. 18. Density profiles of example BLT states on infinite tilings for the (a), (b) 5-fold tiling at $\phi = 0.69\phi_0$; (c), (d) 7-fold tiling at $\phi = 0.4\phi_0$; (e), (f) 10-fold tiling at $\phi = 0.69\phi_0$; and (g), (h) 12-fold tiling at $\phi = 0.4\phi_0$. Each state corresponds to an energy value (shown error bounds) of (a) $E = -3.042\,941\,5 \pm 10^{-7}$ J, (b) $E = -1.395\,230 \pm 2 \times 10^{-6}$ J, (c) $E = -1.238\,795\,796\,461\,629 \pm 5 \times 10^{-15}$ J, (d) $E = -0.872\,060\,288\,846\,29 \pm 10^{-14}$ J, (e) $E = -0.890\,609\,926\,45 \pm 6 \times 10^{-11}$ J, (f) $E = -0.1411 \pm \times 10^{-4}$ J, (g) $E = -1.053\,735\,881\,521\,5 \pm 4 \times 10^{-13}$ J, and (h) $E = -0.598\,18 \pm 2 \times 10^{-5}$ J. All of the states shown have a nonzero effective Chern marker, and are therefore BLT states with in-gap characteristics.

of states on other vertex models has the rotational symmetry consistent with the tiling itself. We also confirm that BLT states can exist in systems with extreme deformations, as shown in Fig. 19. All the states shown in Figs. 18 and 19 have nonzero effective Chern markers and, hence, will support transport in the bulk.

We also plot the infinite-size Hofstadter butterfly for the fivefold lattice in Fig. 20, labeled according to the effective Chern marker. This again demonstrates the removal of conventional ESs from the spectra of the fivefold vertex model and the retention of BLT states across a broad range of flux. In other words, the appearance of BLT states is not limited to

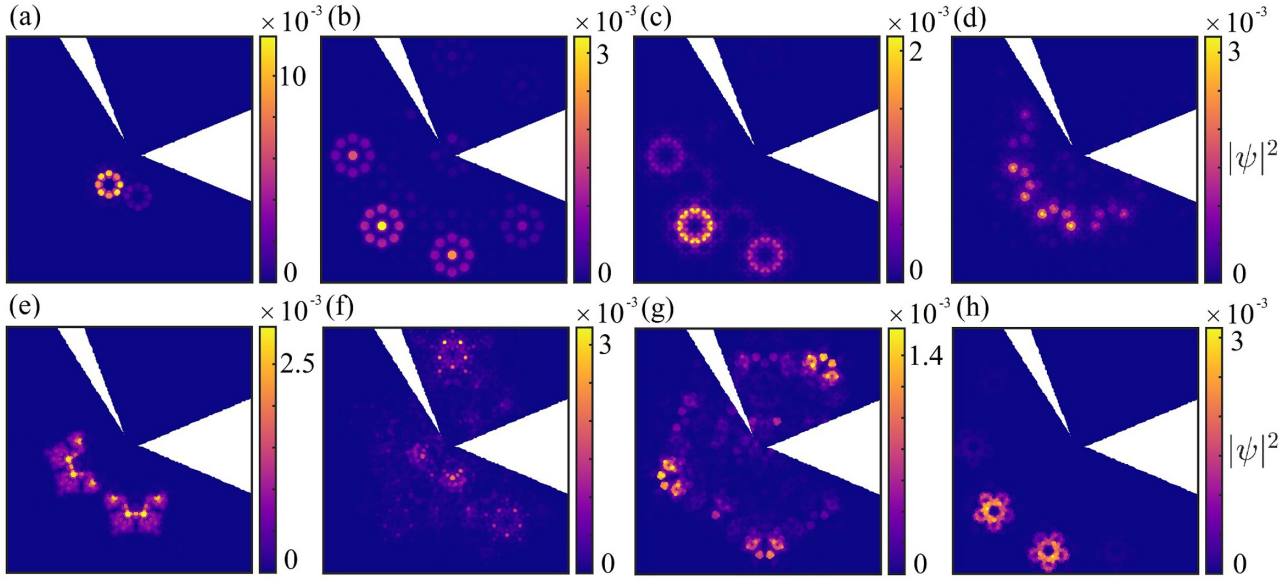

FIG. 19. Density profiles of example BLT states on infinite tilings for the symmetry broken (a)–(d) 8-fold tiling and (e)–(h) 5-fold tiling. We consider fluxes of (a), (b) $\phi = 0.69\phi_0$; (c), (d) $\phi = 0.20\phi_0$; (e), (f) $\phi = 0.69\phi_0$; and (g), (h) $\phi = 0.4\phi_0$. Each state corresponds to an energy value (with shown error bounds) of (a) $E = -1.609\,378 \pm 3 \times 10^{-6}$, (b) $E = -0.7533 \pm 2 \times 10^{-4}$, (c) $E = 1.701\,26 \pm 4 \times 10^{-5}$, (d) $E = 0.9913 \pm 4 \times 10^{-4}$, (e) $E = 0.560\,996 \pm 11 \times 10^{-6}$, (f) $E = 2.1235 \pm 4 \times 10^{-4}$, (g) $E = -1.5209 \pm 3 \times 10^{-4}$, and (h) $E = -1.394\,57 \pm 7 \times 10^{-5}$. All states shown have a nonzero effective Chern marker, and are therefore BLT states with in-gap characteristics.

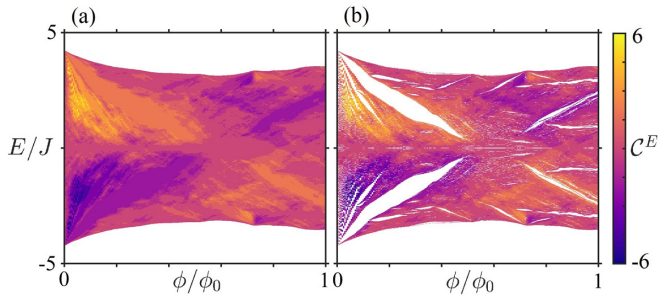

FIG. 20. Effective Chern markers for the infinite 5-fold Moore-Penrose tiling, showing (a) the effective $\mathcal{C}^E$ over a range of energy values E, and (b) a restricted range over values in the spectrum of the infinite lattice (up to the tolerance 0.01). States in (b) with $\mathcal{C}^E \neq 0$ correspond to BLT states.

particular values of the magnetic field or the exact geometry of the lattice, and BLT states can dominate the spectra of quasicrystals, as long as the magnetic aperiodicity is retained. As with their counterparts for the AB vertex model, the BLT states for other quasicrystals do indeed support transport, as shown in Fig. 21 for the 5- and 12-fold examples.

APPENDIX C: FORMATION OF BLT STATES IN A TOY MODEL

In this Appendix, we characterize how these states form through a toy model. First, we consider a simple but misguided toy model that shows the BLT states are not formed by effective edges from the varying local coordination number. These are equivalent to dislocations being present in the system. We then describe a simple toy model showing that the BLT states arise due to the interplay of the quasiperiodic lattice, and mainly the irrational areas present, with the constant magnetic field.

1. Dislocation toy model

At first glance, one might think that BLT states form due to the quasicrystalline nature of the lattice alone. This would be through effective edges being formed in the system via the local aperiodic variation in the coordination number for each site. In many ways, this would be similar to edge states being bound to a dislocation or defect in the lattice structure. Therefore, we consider a toy model on a square lattice with a central region with lattice constant $l_2 = \frac{13\tau}{10}$, where τ is the golden ratio, and an outer region of lattice constant $l_1 = 1$. The lattice constants l_1 and l_2 are incommensurate and lead to a dislocation along the boundary of these two lattices shown in Fig. 22(a). We couple all sites along this dislocation that are within $1.5l_1$ of each other. The dislocation is along the interface where the coordination number varies.

Some examples of the states along the dislocation are shown in Fig. 23. The density profiles of these states look similar to those of the BLT states but with a crystalline fourfold rotational symmetry, as expected for this toy model. They also have a corresponding nonzero Bott index and are, therefore, in-gap and will support transport. However, the local Chern marker shows a striking difference from the BLT states in the quasicrystal. The states along the dislocation are a product of the change of the local Chern marker across the dislocation. This in itself is not a surprise and is usually the reason why in-gap states appear on internal edges in these systems [47–49]. It is clear, however, that this is not how the BLT states form, as we do not see any change in the local Chern marker across the interface for quasicrystalline BLT states. Therefore, even though at first glance the variation in the coordination number

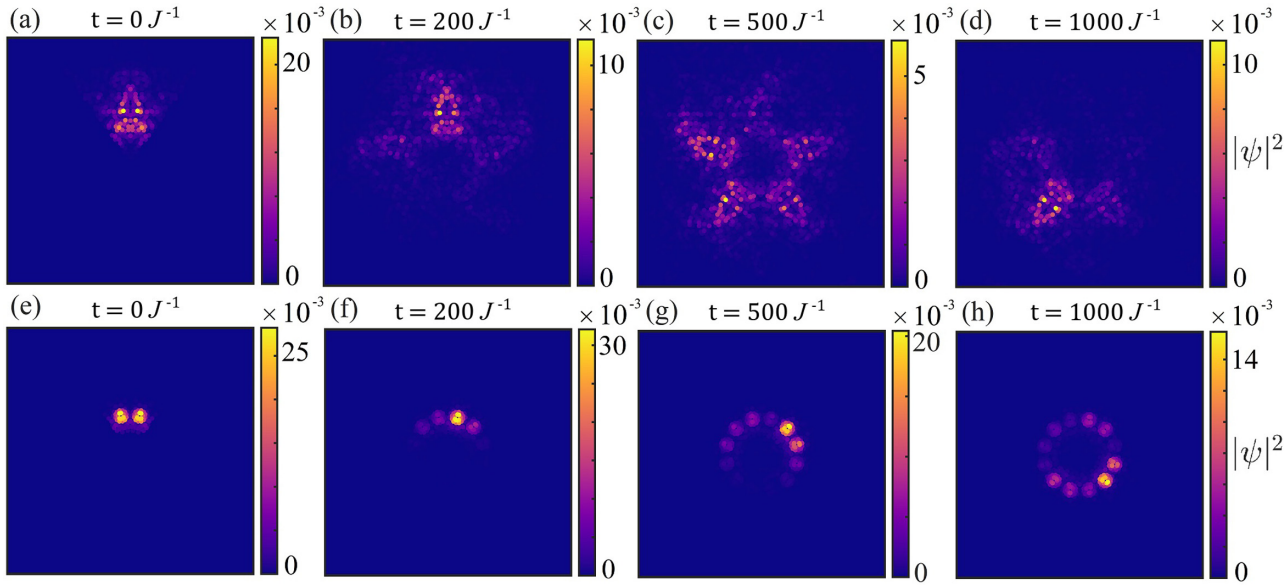

FIG. 21. Infinite-size dynamical transport due to the presence of BLT states for other quasicrystals at time $t = 0$ J^{-1} (first column), $t = 200$ J^{-1} (second column), $t = 500$ J^{-1} (third column), and $t = 1000$ J^{-1} (fourth column). The first row corresponds to the 5-fold BLT state in Fig. 18(b), with $\phi = 0.69\phi_0$. The second row corresponds to an excitation of the 12-fold BLT state in Fig. 18(g), with $\phi = 0.4\phi_0$.

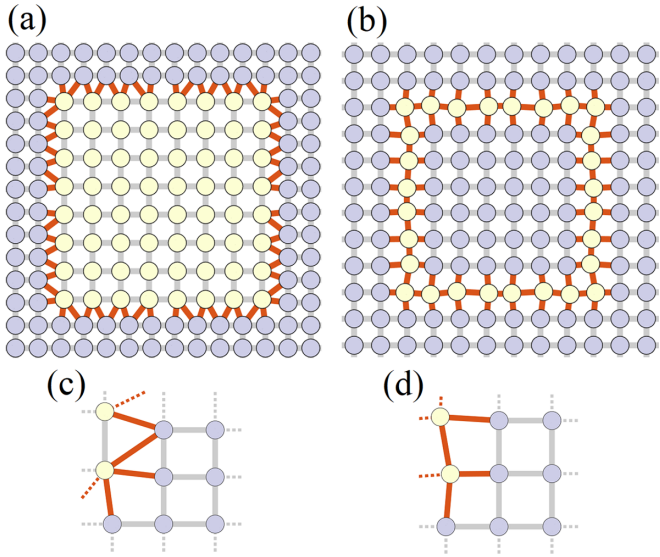

FIG. 22. Zoomed-in portions of the square lattice toy models used to look at the formation of BLT states. In (a), we show a square lattice with period $l_2 = \frac{13\tau}{10}$ embedded in a larger square lattice of period $l_1 = 1$. Connections, colored red, are generated between the boundaries of both lattices that are less than a threshold of $1.5l_1$ apart, resulting in a coordination number dislocation. In (b), we show a square lattice with lattice spacing l that has a positional disorder applied to a selection of sites. The sites colored yellow are randomized from their original position in a small radius of $0.25l$ units. The bottom row of figures (c), (d) shows the bottom right corners of the same lattices in order to emphasize the incommensurate areas between different unit cells more clearly.

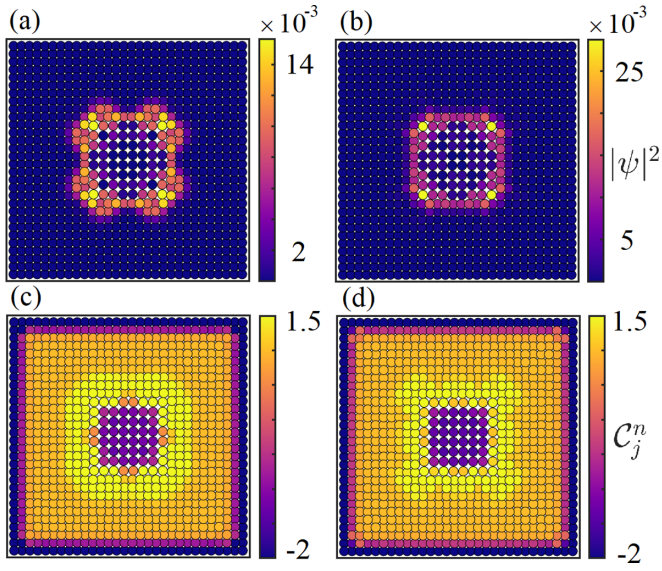

FIG. 23. Example states from the spectrum of the model in Fig. 22(a) with $\phi = 0.84\phi_0$ (a), (b) form across a dislocation and their (c), (d) $\mathcal{C}_j^n$ distributions. For each case, the corresponding Bott indices are (a) $\mathcal{B} = 1$ and (b) $\mathcal{B} = 1$. The $\mathcal{C}_j^n$ distributions are saturated between 1.5 and -2 for visual clarity. Each state also supports a separate bulk effective Chern marker within the inner square lattice, which is sign-flipped.

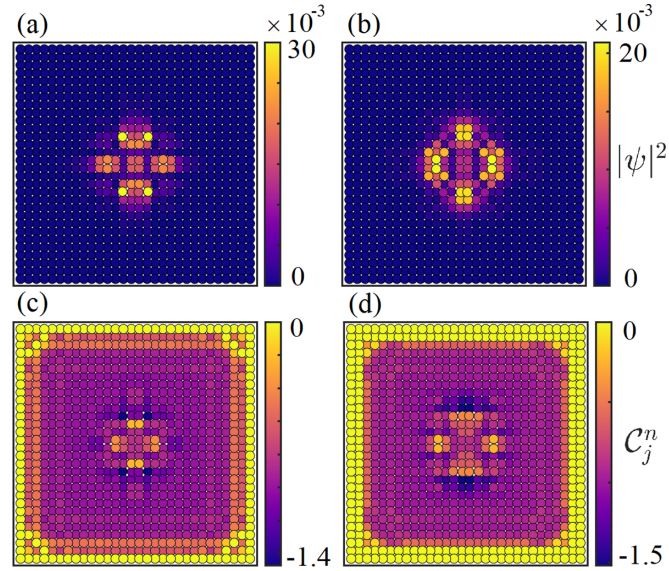

FIG. 24. Example states from the spectrum of the model in Fig. 22(b) with $\phi = 0.70\phi_0$ (a), (b) form around disordered fluxes and their (c), (d) $\mathcal{C}_j^n$ distributions. For each case, the corresponding Bott indices are (a) $\mathcal{B} = -1$ and (b) $\mathcal{B} = -1$. The $\mathcal{C}_j^n$ distributions have the maximum value saturated to 0 for visual clarity.

appears to map well to how the BLT states are formed, it cannot be their true origin.

2. Magnetic aperiodicity toy model

The formation of BLT states is due to an interplay of the magnetic field with the aperiodicity of the quasicrystalline structure. This is to be expected from the results in Sec. IV B, where the location of the BLT states was shown to be largely dependent upon the applied magnetic field strength. Through another toy model on an originally square lattice, we now show that the magnetic aperiodicity introduced into the system is responsible for forming BLT states. In this model, we take a subset of lattice sites on a square perimeter and vary their location to a small degree, while retaining the constant coordination number and connectivity of the square lattice. An example of this toy model is shown in Fig. 22(b), where we also enforce a twofold rotational symmetry for comparison. This toy model has a small region with disorder in the area of tiles. This then maps to disorder in the flux penetrating tiles in this region, as we have cells with irrational areas to each other.

Some examples of the states along the magnetically disordered region are shown in Fig. 24. The states and their corresponding local Chern markers look very similar to the BLT states observed throughout this work. As expected, the states also have a twofold rotational symmetry and show clearly that the formation of BLT states is due to the interplay of the constant magnetic field with the aperiodic structure of the lattice. This also explains why BLT states were not observed before in quasicrystals composed of a single tile such as the Rauzy tiling [38,72], as there is then no magnetic aperiodicity introduced into the system. Note, the Rauzy tiling does have a local variation in the coordination number, further supporting the conclusions from the dislocation toy model. It is also worth noting that if periodic boundary conditions

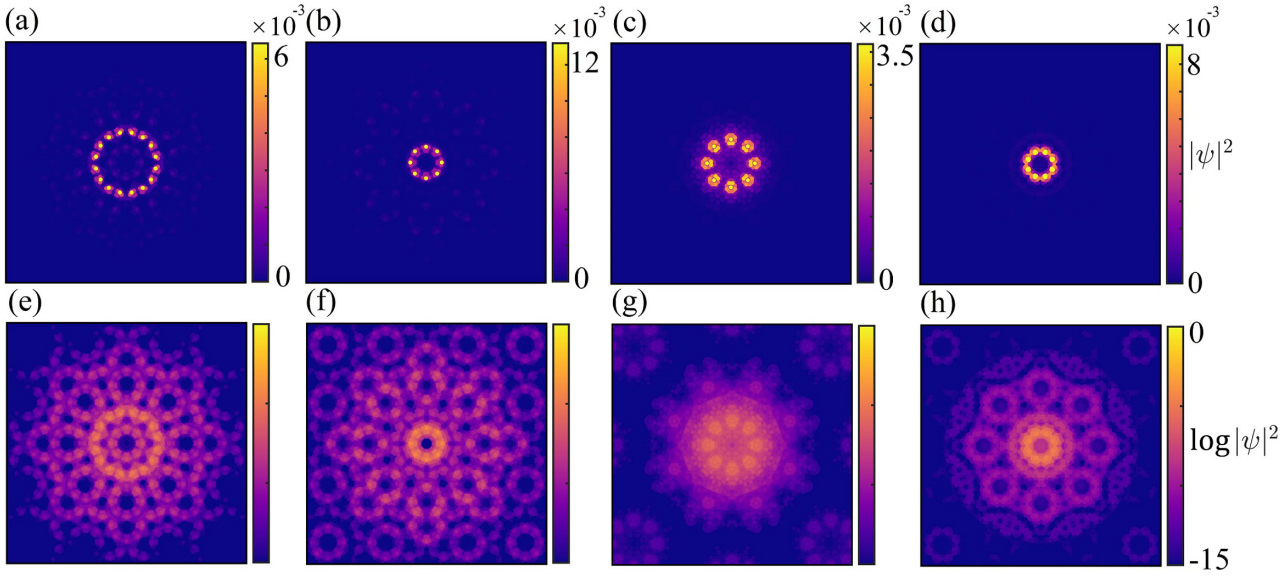

FIG. 25. Density profiles of example BLT states on the infinite AB tiling for (a)–(b), (e)–(f) $\phi = 0.69\phi_0$, (c), (g) $\phi = 0.2\phi_0$, and (d), (h) $\phi = 0.8\phi_0$. The first row of figures plots the real-space density profile, whereas the second row plots the density profile on a log scale. Each state corresponds to an energy value (with shown error bounds) of (a), (e) $E = -0.987\,30 \pm 3 \times 10^{-5}$ J equivalent to Fig. 9(a); (b), (f) $E = -0.974\,79 \pm 2 \times 10^{-5}$ J equivalent to Fig. 9(b); (c), (g) $E = -0.977\,43 \pm 2 \times 10^{-5}$ J equivalent to Fig. 9(c); and (d), (h) $E = -0.997\,183 \pm 5 \times 10^{-6}$ J equivalent to Fig. 9(f). This shows that most BLT states are not strictly localized to a small set of lattice sites.

are applied to the hard edges of these toy models, then the BLT states remain persistent in the spectra. In other words, this again demonstrates that the formation of BLT states is not linked to the presence or geometry of the system's boundary.

Finally, we also note that we have confirmed the presence of other kinds of in-gap states for systems with two incommensurate tiles distributed in a periodic, superlattice arrangement, such as one of the models considered in Fig. 6 of Ref. [43]. However, these states are of a different character from that of the BLT states, as they will typically possess striped and periodic density profiles. This contrasts the usual characteristics of BLT states, which are instead strongly localized to specific regions of the lattice, and not extended. Furthermore, this also confirms that a magnetic aperiodicity is the crucial ingredient necessary to observe BLT states, rather than incommensurate tiles alone. The further study of the possible links between localized in-gap states in periodic, quasicrystalline, and disordered systems could be an interesting area of future research.

APPENDIX D: LOCALIZATION OF BLT STATES

In this Appendix, we briefly consider the localization properties of BLT states for the AB quasicrystal. From the inverse participation ratios IPR^n in Figs. 10(e) and 10(f), it is clear that the vast majority of BLT states are not strictly localized to a small set of lattice sites. In Fig. 25, we plot several density profiles of infinite-size BLT states, including the density profile on a log scale. Here, we can immediately see that, despite the heavy localization of BLT states, they possess an interesting, extended structure of fluctuations throughout a large extent of the lattice. Since there is finite support across large domains of the lattice, this also explains why the inverse participation ratio IPR^n will fluctuate around small, nonzero values.

We note that while the log-scale plots give an impression that the shown BLT states are in fact extended in nature, the values of the state in this extended component are crucial. For the most part, the extended regions of the shown BLT states in Fig. 25, and for all cases we have observed, are below $|\psi|^2 \sim 10^{-7}$. This impacts the physics in two crucial ways. For one, any experiment would need to be repeated over an unreasonably large amount of time or have the ability to differentiate between such different scales. Secondly, when the state is initially localized to the main support of the BLT states, it will only expand into the extended region very slowly, and in effect the timescales of the dynamics within the localised and extended components would be decoupled in a similar way to the Born-Oppenheimer approximation.

[1] H. M. Rosenberg, *The Solid State*, 3rd ed. (Oxford University Press, Oxford, 1988), pp. 124–142.

[2] G. H. Wannier, *Elements of Solid State Theory* (Cambridge University Press, Cambridge, 1959), pp. 130–165.

[3] M. Z. Hasan and C. L. Kane, Rev. Mod. Phys. **82**, 3045 (2010).

[4] A. Bansil, H. Lin, and T. Das, Rev. Mod. Phys. **88**, 021004 (2016).

[5] J. K. Asbóth, L. Oroszlány, and A. Pályi, *A Short Course on Topological Insulators: Band Structure and Edge States in One and Two Dimensions*, Lecture Notes in Physics (Springer, Berlin, 2016), Vol. 919, pp. 23–44.

[6] D. J. Thouless, M. Kohmoto, M. P. Nightingale, and M. den Nijs, Phys. Rev. Lett. **49**, 405 (1982).

[7] M. Aidelsburger, M. Lohse, C. Schweizer, M. Atala, J. T. Barreiro, S. Nascimbène, N. Cooper, I. Bloch, and N. Goldman, Nat. Phys. **11**, 162 (2015).

[8] D. R. Hofstadter, Phys. Rev. B **14**, 2239 (1976).

[9] H. Aoki, M. Ando, and H. Matsumura, Phys. Rev. B **54**, R17296 (1996).

[10] S. İslamoğlu, M. O. Oktel, and O. Gülseren, Phys. Rev. B **85**, 235414 (2012).

[11] F. Harper, S. H. Simon, and R. Roy, Phys. Rev. B **90**, 075104 (2014).

[12] F. Yılmaz and M. Ö. Oktel, Phys. Rev. A **95**, 063628 (2017).

[13] C. W. Duncan, P. Öhberg, and M. Valiente, Phys. Rev. B **97**, 195439 (2018).

[14] L. Du, Q. Chen, A. D. Barr, A. R. Barr, and G. A. Fiete, Phys. Rev. B **98**, 245145 (2018).

[15] L. Wang, H.-H. Hung, and M. Troyer, Phys. Rev. B **90**, 205111 (2014).

[16] G. Möller and N. R. Cooper, Phys. Rev. Lett. **115**, 126401 (2015).

[17] M. E. Tai, A. Lukin, M. Rispoli, R. Schittko, T. Menke, D. Borgnia, P. M. Preiss, F. Grusdt, A. M. Kaufman, and M. Greiner, Nature (London) **546**, 519 (2017).

[18] M. Gerster, M. Rizzi, P. Silvi, M. Dalmonte, and S. Montangero, Phys. Rev. B **96**, 195123 (2017).

[19] J. Dalibard, F. Gerbier, G. Juzeliūnas, and P. Öhberg, Rev. Mod. Phys. **83**, 1523 (2011).

[20] I. Bloch, J. Dalibard, and S. Nascimbene, Nat. Phys. **8**, 267 (2012).

[21] C. R. Dean, L. Wang, P. Maher, C. Forsythe, F. Ghahari, Y. Gao, J. Katoch, M. Ishigami, P. Moon, M. Koshino, T. Taniguchi, K. Watanabe, K. L. Shepard, J. Hone, and P. Kim, Nature (London) **497**, 598 (2013).

[22] S. Mukherjee, A. Spracklen, M. Valiente, E. Andersson, P. Öhberg, N. Goldman, and R. R. Thomson, Nat. Commun. **8**, 13918 (2017).

[23] D. Shechtman, I. Blech, D. Gratias, and J. W. Cahn, Phys. Rev. Lett. **53**, 1951 (1984).

[24] D. Levine and P. J. Steinhardt, Phys. Rev. Lett. **53**, 2477 (1984).

[25] T. Ishimasa, H.-U. Nissen, and Y. Fukano, Phys. Rev. Lett. **55**, 511 (1985).

[26] T. Janssen, G. Chapuis, and M. De Boissieu, *Aperiodic Crystals: From Modulated Phases to Quasicrystals: Structure and Properties*, 2nd ed. (Oxford University Press, Oxford, 2018), pp. 305–405.

[27] T. Janssen, Dynamics and transport properties of aperiodic crystals, in *From Quasicrystals to More Complex Systems*, edited by F. Axel, F. Denoyer, and J. P. Gazeau (Springer-Verlag, Berlin, 2000), pp. 1–22.

[28] C. Berger and T. Grenet, Electronic properties of quasicrystals. A comparison with approximant phases and disordered systems, in *From Quasicrystals to More Complex Systems*, edited by F. Axel, F. Denoyer, and J. P. Gazeau (Springer-Verlag, Berlin, 2000), pp. 49–83.

[29] S. Gopalakrishnan, I. Martin, and E. A. Demler, Phys. Rev. Lett. **111**, 185304 (2013).

[30] P. Bordia, H. Lüschen, S. Scherg, S. Gopalakrishnan, M. Knap, U. Schneider, and I. Bloch, Phys. Rev. X **7**, 041047 (2017).

[31] K. G. H. Viebahn, Quasicrystalline optical lattices for ultracold atoms, Ph.D. thesis, University of Cambridge (2018).

[32] K. Viebahn, M. Sbroscia, E. Carter, J.-C. Yu, and U. Schneider, Phys. Rev. Lett. **122**, 110404 (2019).

[33] S. J. Ahn, P. Moon, T.-H. Kim, H.-W. Kim, H.-C. Shin, E. H. Kim, H. W. Cha, S.-J. Kahng, P. Kim, M. Koshino, Y.-W. Son, C.-W. Yang, and J. R. Ahn, Science **361**, 782 (2018).

[34] B. Freedman, G. Bartal, M. Segev, R. Lifshitz, D. N. Christodoulides, and J. W. Fleischer, Nature (London) **440**, 1166 (2006).

[35] M. A. Bandres, M. C. Rechtsman, and M. Segev, Phys. Rev. X **6**, 011016 (2016).

[36] Y. An, Z. Gao, and Z. Ouyang, Appl. Phys. Lett. **116**, 151104 (2020).

[37] T. Hatakeyama and H. Kamimura, J. Phys. Soc. Jpn. **58**, 260 (1989).

[38] D.-T. Tran, A. Dauphin, N. Goldman, and P. Gaspard, Phys. Rev. B **91**, 085125 (2015).

[39] J.-N. Fuchs and J. Vidal, Phys. Rev. B **94**, 205437 (2016).

[40] J.-N. Fuchs, R. Mosseri, and J. Vidal, Phys. Rev. B **98**, 165427 (2018).

[41] H. Huang and F. Liu, Phys. Rev. Lett. **121**, 126401 (2018).

[42] H. Huang and F. Liu, Phys. Rev. B **98**, 125130 (2018).

[43] C. W. Duncan, S. Manna, and A. E. B. Nielsen, Phys. Rev. B **101**, 115413 (2020).

[44] R. Chen, C.-Z. Chen, J.-H. Gao, B. Zhou, and D.-H. Xu, Phys. Rev. Lett. **124**, 036803 (2020).

[45] C.-B. Hua, R. Chen, B. Zhou, and D.-H. Xu, Phys. Rev. B **102**, 241102(R) (2020).

[46] D. Varjas, A. Lau, K. Pöyhönen, A. R. Akhmerov, D. I. Pikulin, and I. C. Fulga, Phys. Rev. Lett. **123**, 196401 (2019).

[47] M. Brzezińska, A. M. Cook, and T. Neupert, Phys. Rev. B **98**, 205116 (2018).

[48] S. Pai and A. Prem, Phys. Rev. B **100**, 155135 (2019).

[49] S. Sarangi and A. E. Nielsen, Phys. Rev. B **104**, 045147 (2021).

[50] Y. Ran, Y. Zhang, and A. Vishwanath, Nat. Phys. **5**, 298 (2009).

[51] F.-F. Li, H.-X. Wang, Z. Xiong, Q. Lou, P. Chen, R.-X. Wu, Y. Poo, J.-H. Jiang, and S. John, Nat. Commun. **9**, 1 (2018).

[52] M. Valiente, arXiv:1907.08215.

[53] Q. Wang, H. Xue, B. Zhang, and Y. D. Chong, Phys. Rev. Lett. **124**, 243602 (2020).

[54] S.-S. Diop, L. Fritz, M. Vojta, and S. Rachel, Phys. Rev. B **101**, 245132 (2020).

[55] V. Juričić, A. Mesaros, R.-J. Slager, and J. Zaanen, Phys. Rev. Lett. **108**, 106403 (2012).

[56] R.-J. Slager, A. Mesaros, V. Juričić, and J. Zaanen, Phys. Rev. B **90**, 241403(R) (2014).

[57] R.-J. Slager, L. Rademaker, J. Zaanen, and L. Balents, Phys. Rev. B **92**, 085126 (2015).

[58] R.-J. Slager, J. Phys. Chem. Solids **128**, 24 (2019).

[59] M. J. Colbrook, B. Roman, and A. C. Hansen, Phys. Rev. Lett. **122**, 250201 (2019).

[60] B. Grünbaum and G. C. Shephard, *Tilings and Patterns* (Dover, Mineola, NY, 2016), pp. 15–165.

[61] M. Baake, A guide to mathematical quasicrystals, in *Quasicrystals: An Introduction to Structure, Physical Properties and Applications*, edited by J.-B. Suck, M. Schreiber, and P. Häussler (Springer, Berlin, 2002), pp. 17–48.

[62] R. Penrose, Bull. Inst. Math. Appl. **10**, 266 (1974).
[63] E. Cockayne, Random tiling models for quasicrystals, in *From Quasicrystals to More Complex Systems*, edited by F. Axel, F. Denoyer, and J. P. Gazeau (Springer-Verlag, Berlin, 2000), pp. 115–143.
[64] J. E. S. Socolar, Phys. Rev. B **39**, 10519 (1989).
[65] J. C. Lagarias, Commun. Math. Phys. **179**, 365 (1996).
[66] Z. Masáková, J. Patera, and E. Pelantová, J. Phys. A **31**, 1443 (1998).
[67] T. Rieth and M. Schreiber, Phys. Rev. B **51**, 15827 (1995).
[68] T. C. Choy, Phys. Rev. Lett. **55**, 2915 (1985).
[69] P. Repetowicz, U. Grimm, and M. Schreiber, Phys. Rev. B **58**, 13482 (1998).
[70] E. de Prunelé, Phys. Rev. B **66**, 094202 (2002).
[71] R. Peierls, in *Selected Scientific Papers Of Sir Rudolf Peierls: (With Commentary)* (World Scientific, Singapore, 1997), pp. 97–120.
[72] J. Vidal and R. Mosseri, J. Non-Cryst. Solids **334–335**, 130 (2004).
[73] J. Herzog-Arbeitman, Z.-D. Song, N. Regnault, and B. A. Bernevig, Phys. Rev. Lett. **125**, 236804 (2020).
[74] M. J. Colbrook, The foundations of infinite-dimensional spectral computations, Ph.D. thesis, University of Cambridge (2020).
[75] M. J. Colbrook and A. C. Hansen, arXiv:1908.09592 [J. Eur. Math. Soc. (to be published)].
[76] M. J. Colbrook, arXiv:1908.09598.
[77] M. Valiente, C. W. Duncan, and N. T. Zinner, J. Phys. B **54**, 065301 (2021).
[78] M. J. Colbrook, IMA Mathematics Today (2021), https://ima.org.uk/16912/unscrambling-the-infinite-can-we-compute-spectra/.
[79] M. J. Colbrook, A. Horning, K. Thicke, and A. B. Watson, arXiv:2112.03942.
[80] Z. Wang, X.-L. Qi, and S.-C. Zhang, New J. Phys. **12**, 065007 (2010).
[81] D. Toniolo, Phys. Rev. B **98**, 235425 (2018).
[82] R. Bianco and R. Resta, Phys. Rev. B **84**, 241106(R) (2011).
[83] Q.-B. Zeng, Y.-B. Yang, and Y. Xu, Phys. Rev. B **101**, 020201(R) (2020).
[84] T. A. Loring and M. B. Hastings, Europhys. Lett. **92**, 67004 (2010).
[85] X. S. Wang, A. Brataas, and R. E. Troncoso, Phys. Rev. Lett. **125**, 217202 (2020).
[86] H. D. Cornean, I. Herbst, and G. Nenciu, Ann. Henri Poincaré **17**, 3361 (2016).
[87] E. Cancés, A. Levitt, G. Panati, and G. Stoltz, Phys. Rev. B **95**, 075114 (2017).
[88] G. Panati, Ann. Henri Poincaré **8**, 995 (2007).
[89] F. Song, S. Yao, and Z. Wang, Phys. Rev. Lett. **123**, 246801 (2019).
[90] M. D. Caio, G. Möller, N. R. Cooper, and M. Bhaseen, Nat. Phys. **15**, 257 (2019).
[91] B. Irsigler, J.-H. Zheng, and W. Hofstetter, Phys. Rev. A **100**, 023610 (2019).
[92] Y. Kuno, Phys. Rev. B **100**, 054108 (2019).
[93] M. Reed and B. Simon, *Methods of Modern Mathematical Physics. I*, 2nd ed. (Academic, New York, 1980), pp. xv+400.
[94] M. J. Colbrook, Commun. Math. Phys. **384**, 433 (2021).
[95] M. J. Colbrook, A. Horning, and A. Townsend, SIAM Rev. **63**, 489 (2021).
[96] M. J. Colbrook and A. Horning, arXiv:2201.01314.
[97] M. J. Colbrook, SIAM J. Numer. Anal. **60**, 396 (2022).
[98] M. Ostmann, J. Minář, M. Marcuzzi, E. Levi, and I. Lesanovsky, New J. Phys. **19**, 123015 (2017).
[99] L. Madail, S. Flannigan, A. M. Marques, A. J. Daley, and R. G. Dias, Phys. Rev. B **100**, 125123 (2019).
[100] D. Guéry-Odelin, A. Ruschhaupt, A. Kiely, E. Torrontegui, S. Martínez-Garaot, and J. G. Muga, Rev. Mod. Phys. **91**, 045001 (2019).
[101] Y. Hatsugai, T. Fukui, and H. Aoki, Phys. Rev. B **74**, 205414 (2006).
[102] I. L. Garanovich, S. Longhi, A. A. Sukhorukov, and Y. S. Kivshar, Phys. Rep. **518**, 1 (2012).
[103] Y. Lumer, M. A. Bandres, M. Heinrich, L. J. Maczewsky, H. Herzig-Sheinfux, A. Szameit, and M. Segev, Nat. Photon. **13**, 339 (2019).
[104] N. Goldman, J. Dalibard, M. Aidelsburger, and N. R. Cooper, Phys. Rev. A **91**, 033632 (2015).
[105] J. Guglielmon, M. C. Rechtsman, and M. I. Weinstein, Phys. Rev. A **103**, 013505 (2021).
[106] D. Johnstone, P. Öhberg, and C. W. Duncan, Phys. Rev. A **100**, 053609 (2019).
[107] D. Johnstone, P. Öhberg, and C. W. Duncan, J. Phys. A **54**, 395001 (2021).
[108] R. Gautier, H. Yao, and L. Sanchez-Palencia, Phys. Rev. Lett. **126**, 110401 (2021).
[109] U. Schollwöck, Ann. Phys. **326**, 96 (2011).
[110] R. Orús, Ann. Phys. **349**, 117 (2014).
[111] P. Silvi, F. Tschirsich, M. Gerster, J. Jünemann, D. Jaschke, M. Rizzi, and S. Montangero, SciPost Phys. Lect. Notes 8 (2019).
[112] D. Xiao, M.-C. Chang, and Q. Niu, Rev. Mod. Phys. **82**, 1959 (2010).
[113] N. Lang and H. P. Büchler, npj Quantum Inf. **3**, 47 (2017).
[114] D. Johnstone, M. J. Colbrook, A. E. B. Nielsen, P. Öhberg, and C. W. Duncan, Data for "Bulk localised transport in infinite and finite quasicrystals via magnetic aperiodicity", University of Strathclyde, doi: 10.15129/14c3c730-a959-468f-8e72-30bbabf2540e (2022).
[115] J. Ben-Artzi, M. J. Colbrook, A. C. Hansen, O. Nevanlinna, and M. Seidel, arXiv:1508.03280.